

Robust Wannierization including magnetization and spin-orbit coupling via projectability disentanglement

Yuhao Jiang,^{1,2} Junfeng Qiao,³ Nataliya Paulish,¹ Weisheng Zhao,^{2,4,*} Nicola Marzari,^{1,3} and Giovanni Pizzi^{1,3,†}

¹*PSI Center for Scientific Computing, Theory and Data, 5232 Villigen PSI, Switzerland*

²*Fert Beijing Institute, School of Integrated Circuit Science and Engineering, Beihang University, 100191 Beijing, China*

³*Theory and Simulations of Materials (THEOS),*

and National Centre for Computational Design and Discovery of Novel Materials (MARVEL),

École Polytechnique Fédérale de Lausanne, 1015 Lausanne, Switzerland

⁴*National Key Lab of Spintronics, Institute of International Innovation, Beihang University, 311115 Hangzhou, China*

Maximally-localized Wannier functions (MLWFs) are widely employed as an essential tool for calculating the physical properties of materials due to their localized nature and computational efficiency. Projectability-disentangled Wannier functions (PDWFs) have recently emerged as a reliable and efficient approach for automatically constructing MLWFs that span both occupied and lowest unoccupied bands. Here, we extend the applicability of PDWFs to magnetic systems and/or those including spin-orbit coupling, and implement such extensions in automated workflows. Furthermore, we enhance the robustness and reliability of constructing PDWFs by defining an extended protocol that automatically expands the projectors manifold, when required, by introducing additional appropriate hydrogenic atomic orbitals. We benchmark our extended protocol on a set of 200 chemically diverse materials, as well as on the 40 systems with the largest band distance obtained with the standard PDWF approach, showing that on our test set the present approach delivers a 100% success rate in obtaining accurate Wannier-function interpolations, i.e., an average band distance below 15 meV between the DFT and Wannier-interpolated bands, up to 2 eV above the Fermi level.

I. INTRODUCTION

In materials science calculations, density-functional theory (DFT) [1] is nowadays an established and highly versatile method, widely used for calculating various physical properties of extended systems and molecules. However, to accurately capture several properties of crystalline materials, such as for instance the anomalous Hall effect [2] or the spin Hall effect [3, 4], calculations on a very dense k -point mesh in the Brillouin zone are required, often involving even millions of k -points [5, 6] to achieve convergence. Solving the Kohn-Sham equations [7] independently for such an extensive number of k -points incurs significant computational cost.

An alternative approach is to construct a tight-binding model using a real-space basis of Wannier functions (WFs) [8], which are efficiently obtained from Bloch functions via a unitary transformation between the Bloch wavefunctions at every k -point, and then Fourier-transformed to generate maximally localized Wannier functions (MLWFs) [9]. These functions allow for efficient interpolation of wavefunctions onto arbitrary k -point meshes at a low computational cost. This approach has been widely adopted in particular for calculating physical quantities requiring extensive k -point integration [10], such as the density of states (DOS) [11], Boltzmann transport [12], anomalous Hall effect [13], orbital magnetic moments [14], and the spin Hall effect [15, 16].

WFs $|w_{n\mathbf{R}}\rangle$ are obtained via a Fourier transformation of the Bloch states $|\psi_{n\mathbf{k}}\rangle$ associated to the same band n ,

$$|w_{n\mathbf{R}}\rangle = \frac{V}{(2\pi)^3} \int_{BZ} d\mathbf{k} e^{-i\mathbf{k}\mathbf{R}} |\psi_{n\mathbf{k}}\rangle, \quad (1)$$

where V is the volume of the primitive cell, and \mathbf{k} and \mathbf{R} are the Bloch quasi-momentum in the BZ and a real-space lattice vector, respectively. However, there is a gauge freedom of the Bloch functions where each Bloch state can be multiplied by a phase factor $e^{i\phi_n(\mathbf{k})}$, dependent both on n and \mathbf{k} , without changing the Hilbert space but changing the shape of the WFs (and in particular their localization in real space). MLWFs utilize such a gauge freedom to obtain the most localized WFs [9] by minimizing a quadratic spread functional

$$\Omega = \sum_{n=1}^J [\langle w_{n\mathbf{0}} | \mathbf{r}^2 | w_{n\mathbf{0}} \rangle - |\langle w_{n\mathbf{0}} | \mathbf{r} | w_{n\mathbf{0}} \rangle|^2], \quad (2)$$

where J is the number of target Wannier bands. For multi-band systems, the gauge freedom is further generalized to allow mixing between different bands, rather than being limited to a simple exponential phase factor. This freedom can be encoded in a set of unitary matrices $U_{mn\mathbf{k}}$, so that MLWFs can be expressed as

$$|w_{n\mathbf{R}}\rangle = \frac{V}{(2\pi)^3} \int_{BZ} d\mathbf{k} e^{-i\mathbf{k}\mathbf{R}} \sum_{m=1}^{J_{\mathbf{k}}} |\psi_{m\mathbf{k}}\rangle U_{mn\mathbf{k}}. \quad (3)$$

For an isolated set of bands, such as the valence bands of semiconductors or insulators, $J_{\mathbf{k}}$ is a constant that equals to J , and the $U_{mn\mathbf{k}}$ are unitary square matrices. For metallic systems, where the energy bands are entangled, one should select more bands and perform a disentanglement procedure [17]. The number $J_{\mathbf{k}}$ of selected bands

* weisheng.zhao@buaa.edu.cn

† giovanni.pizzi@psi.ch

is k -dependent, and $U_{m\mathbf{k}}$ are semi-unitary rectangular matrices.

In practice, the algorithm to obtain MLWFs by minimizing Eq. (2) is typically implemented via an iterative algorithm, for which an adequately localized initial guess must be provided. This initial guess needs to be sufficiently close to the final Wannier functions to achieve convergence and, until very recently, its selection required physical intuition. One common approach is to project Bloch functions onto hydrogenic wave functions $|g_n\rangle$ [9], to obtain

$$|\phi_{n\mathbf{k}}\rangle = \sum_{m=1}^{J_{\mathbf{k}}} |\psi_{m\mathbf{k}}\rangle \langle \psi_{m\mathbf{k}} | g_n \rangle. \quad (4)$$

Since the $U_{m\mathbf{k}}$ should be unitary matrices, the projection matrices $A_{m\mathbf{k}} = \langle \psi_{m\mathbf{k}} | g_n \rangle$ are further orthonormalized through the Löwdin orthonormalization algorithm [18] to obtain the starting $U_{m\mathbf{k}}$ matrices for the minimization procedure. Furthermore, for entangled bands the conventional approach [that we label as energy disentanglement (ED)] is to set an energy window to select the disentanglement manifold [17]. An outer window is first defined, including all Bloch states that can be linearly combined to obtain a smaller disentangled manifold. A smaller inner window is then often also used to define frozen states, which are kept unchanged during the disentanglement process. However, this requires manual setting of input parameters, such as the number of bands and target MLWFs, and the parameters determining the shape of hydrogenic projectors, which limits its integration into high-throughput (HT) calculations. Recently, new algorithms have been proposed to address the challenges associated with HT computations [19–22]. Among these, projectability disentanglement (PD) [21] emerged an efficient and accurate algorithm that can be easily automated. The PD method uses a criterion based on the value of the projectability of each state onto a set of localized pseudo-atomic orbitals (PAOs) [23] to determine the selection of bands used to construct the initial guess. Typically, PAOs are extracted from the pseudopotentials used in DFT calculations. In this context, the value of the projectability $p_{m\mathbf{k}}$ refers to the projection of the Bloch wave function $|\psi_{m\mathbf{k}}\rangle$ onto the PAOs $|g_n\rangle$, as expressed by

$$p_{m\mathbf{k}} = \sum_n \langle \psi_{m\mathbf{k}} | g_n \rangle \langle g_n | \psi_{m\mathbf{k}} \rangle. \quad (5)$$

The main idea of the PD method can be summarized as follows: states with projectability $p_{m\mathbf{k}} \approx 1$ are kept unchanged (in such a case, the set of projectors $|g_n\rangle$ is an almost complete set for the Bloch state $|\psi_{m\mathbf{k}}\rangle$); states with projectability $p_{m\mathbf{k}} \approx 0$ can instead be neglected, as they are essentially not included in the space spanned by the projectors. The remaining states are instead combined, as prescribed by the disentanglement procedure, to construct the disentangled manifold.

HT calculations based on PDWFs have demonstrated that this method can efficiently produce highly accurate tight-binding (TB) models [21]. Current automated PDWF implementations have only been performed on spin-unpolarized systems, without considering spin degrees of freedom needed to describe, e.g., ferromagnetic, antiferromagnetic [24, 25] and ferrimagnetic [26] structures. Furthermore, when relativistic effects are also taken into account by introducing spin-orbit coupling (SOC), higher-order magnetic interactions [27, 28], topological structures [29, 30], intricate magnetic structures in real space [31], spin textures in momentums space [32] and other SOC-dominated physical phenomena can be described. Therefore, in this paper we aim to extend the PDWF approach to magnetic systems and requiring SOC. In doing so, we also extend the PDWF algorithm by defining a protocol to introduce additional projections in the form of hydrogenic atomic orbitals. As a result, we enhance the overall robustness of the Wannierization process, achieving a remarkable 100% success rate in obtaining accurate Wannier interpolations for all materials in our test set.

II. RESULTS

To quantitatively measure the quality of the band structures obtained from Wannier interpolation with respect to the DFT band structures, we employ the definitions from Ref. [33] to compute the average band distance

$$\eta_\nu = \sqrt{\frac{\sum_{n\mathbf{k}} \tilde{f}_{n\mathbf{k}} (\epsilon_{n\mathbf{k}}^{\text{DFT}} - \epsilon_{n\mathbf{k}}^{\text{Wan}})^2}{\sum_{n\mathbf{k}} \tilde{f}_{n\mathbf{k}}}} \quad (6)$$

and the maximum band distance

$$\eta_\nu^{\text{max}} = \max_{n\mathbf{k}} \left(\tilde{f}_{n\mathbf{k}} |\epsilon_{n\mathbf{k}}^{\text{DFT}} - \epsilon_{n\mathbf{k}}^{\text{Wan}}| \right), \quad (7)$$

where $\tilde{f}_{n\mathbf{k}} = \sqrt{f_{n\mathbf{k}}^{\text{DFT}}(E_F + \nu, \sigma) f_{n\mathbf{k}}^{\text{Wan}}(E_F + \nu, \sigma)}$ is an effective Fermi-Dirac distribution, and $f(E_F + \nu, \sigma)$ is the Fermi-Dirac distribution for DFT and Wannier interpolated states, with E_F being the Fermi level of the system. In the following, we choose $\nu = 2$ eV and $\sigma = 0.1$ eV (the same as in Ref. [21]) in order to consider band differences only for those bands with energy (approximately) below $E_F + 2$ eV. This includes the valence bands and a few conduction bands near the Fermi level, which are typically the relevant ones to determine most physical properties. Furthermore, in the calculations presented in this work, all computations based on PDWFs were configured with an additional frozen energy window, which was set to include all states up to 2 eV above the Fermi level. This approach (also named PD+ED in Ref. [21]) is the recommended approach when using the PDWF method (see Ref. [21]) as it generally provides higher-quality Wannier interpolation than just using PD with no frozen window.

A. Spin-orbit coupling

SOC, as a relativistic effect, plays a significant role in systems involving heavy elements. It can lift degeneracies [34] and open band gaps at certain k -points where SOC plays a dominant role [35], leading to notable changes in the electronic properties. Relativistic effects are described by the Dirac equation [36], whose solutions are four-component spinors. However, two of these components correspond to antimatter, which is typically neglected in low-energy physics. As a result, SOC is often approximated as a relativistic correction to the Schrödinger equation [37], with wavefunctions described as two-component spinors. The initial projectors for MLWFs should thus align with the physics of SOC. Namely, one wants to use pseudo-atomic orbitals obtained from fully relativistic pseudopotentials. Since currently the SSSP [33] library does not offer a SOC version, we performed our SOC calculations using pseudopotentials from the PseudoDojo 0.4 [38] library, containing norm-conserving fully relativistic pseudopotentials, and conducted validation calculations using the `pslibrary` [39] 1.0.0 (PBE, PAW, fully relativistic). For `pslibrary`, we selected the corresponding pseudopotentials based on the recommendations from Ref. [40]. We note that, for the `pslibrary`, some pseudopotentials for certain elements may either be missing or result in DFT calculations that fail to converge. Consequently, for some elements, we used older versions of `pslibrary` or substituted pseudopotentials from PseudoDojo. Therefore, we refer to this set as a `modified-pslibrary` set in the following text; the specific pseudopotential files used are detailed in Supplementary Table VI.

Due to SOC, the orbital quantum number l and the spin quantum number s are no longer good quantum numbers, and the system is instead described by the total angular momentum quantum number j . Consequently, the projectors become j -dependent when SOC is considered. To extend the workflow to SOC systems, we adjust the number of energy bands and projectors in the SOC system. For the PDWF approach, since the projectors can be directly obtained from the pseudopotential files, we modified the `pw2wannier90.x` code, part of `QUANTUM ESPRESSO` (QE) [41, 42], for projecting from plane-wave functions onto projectors accounting for their dependence on j . Additionally, to enable the functionality of reading projectors from external files as implemented in Ref [21], we also implemented routines for reading j -dependent projectors from external files.

The effect of SOC on the band structure of BCC tungsten, as well as the quality of the Wannier-interpolated bands obtained with our algorithm including SOC, are demonstrated in Fig. 1. Some bands exhibit splitting due to SOC, particularly along the $\Gamma - H$ k -path, where some band crossings transition into anti-crossings induced by SOC just below the Fermi level. The Wannier-interpolated band structure obtained using our extension of the PDWF method displays a η_2 band distance of only

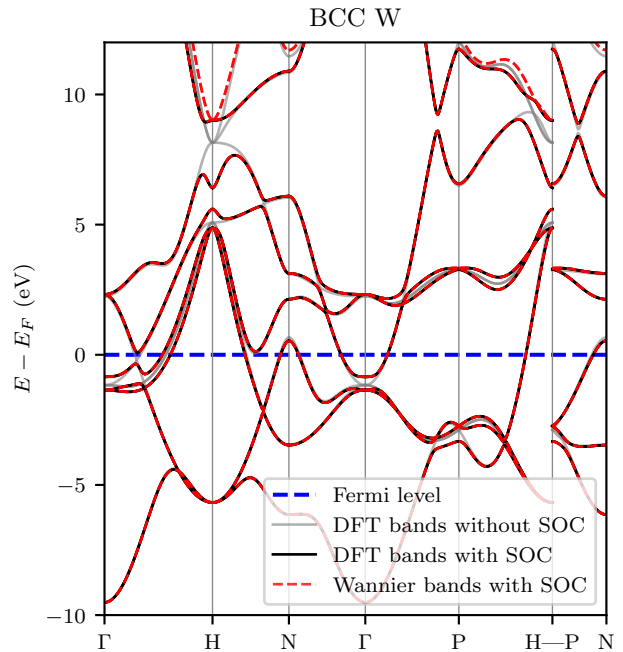


FIG. 1. **Electronic band structure of BCC tungsten.** The gray and black solid lines are the energy bands obtained directly from first-principles DFT calculations without and with SOC, respectively. The red dashed lines are the energy bands obtained from Wannier interpolation with SOC using our extended PDWF method. The Fermi level is marked as a horizontal blue dashed line.

2.24 meV. Notably, even at approximately 8 eV above the Fermi level, the Wannier-interpolated bands remain in good agreement with the DFT bands. Thus, this Wannier tight-binding model is capable of accurately describing the electronic bands of tungsten and is suitable for precise calculations of SOC-related properties.

To further validate our algorithm, we performed Wannierization calculations including SOC on the set of 200 chemically diverse materials extracted from the Materials Cloud 3D crystals database (MC3D) [43] already used for benchmarking in Ref. [21]. 173 among these materials contain elements with atomic numbers greater than 20, where SOC effects become non-negligible. Therefore, this dataset is a also good test set for estimating the accuracy of Wannier interpolation with SOC, and where the few materials containing only light elements enable us to verify that the robustness of the PDWF approach is not disrupted when including SOC effects, even when these are negligible.

To compare the performance of different pseudopotential sets used to obtain PDWFs in the presence of SOC, we computed the band distance η_2 using both the PseudoDojo and the `modified-pslibrary` sets described earlier. The cumulative histogram is shown with dashed lines in Fig. 2. When using PseudoDojo there are 25 cases with band distance η_2 exceeding 20 meV, and the median and mean η_2 are 2.873 meV and 10.136 meV, respec-

tively. When using the **modified-pslibrary** set, there are instead only 7 cases with η_2 larger than 20 meV, with median and mean η_2 being 1.411 meV and 4.597 meV, respectively.

We note that even though both sets of calculations involve the same set of materials, the results exhibit significant differences. Moreover, we still have few materials with large η_2 in both sets. We discuss how to address and solve both these issues (dependence on the pseudopotentials used, and low-quality band interpolation) in the next section, thanks to the inclusion of selected additional hydrogenic projectors. Nevertheless, we highlight that the quality of the results is already quite good, with the **modified-pslibrary** set (including SOC) achieving key metrics (median and mean band distance) comparable to the data from Ref. [21] (PDWF without SOC), and the statistical results of the **PseudoDojo** still outperforming those obtained for HT calculations using the SCDM method [20, 21].

B. Improving Robustness by Adding Hydrogenic Projectors

In this section, we discuss the motivation and effectiveness of extending the projection space by adding external projectors. We first observe that for about 3% of systems (7/200 for mid-throughput calculations and 478/21737 in the case of the HT calculations in Ref. [21]), there remains a relatively large deviation between the Wannier interpolated bands and the DFT bands (band distance η_2 greater than 20 meV). Analogously, our results using the PDWF method extended to SOC also exhibit similar trends, as discussed in the previous section. Furthermore, the statistical results of band distance depend on the pseudopotential sets: as discussed earlier, when using **PseudoDojo**, 25/200 ($\sim 12.5\%$) of the materials have $\eta_2 \geq 20$ meV, while only 7/200 ($\sim 3.5\%$) have $\eta_2 \geq 20$ meV when using the **modified-pslibrary** set. Since physical quantities should not depend on the pseudopotential choice, and since the implementation of the calculation of certain properties may require specific pseudopotentials (e.g., advanced properties might be implemented only for norm-conserving pseudopotentials), it is important to devise algorithms that are largely independent of the underlying pseudopotentials. To address this, we aim to identify the causes of remaining discrepancies between DFT and Wannier-interpolated bands, and design an appropriate algorithm that can be easily applied across various pseudopotential sets, thereby enhancing the reliability and robustness of the PDWF method.

We selected AlCo as an example, for which we computed PDWFs using the **PseudoDojo** set, obtaining a fairly large $\eta_2 = 46.5$ meV. The primary source of the difference between DFT and Wannier bands is along the k -path from R ($1/2, 1/2, 1/2$) to M ($1/2, 1/2, 0$), as shown in Fig. 3(a). Notably, there are significant oscilla-

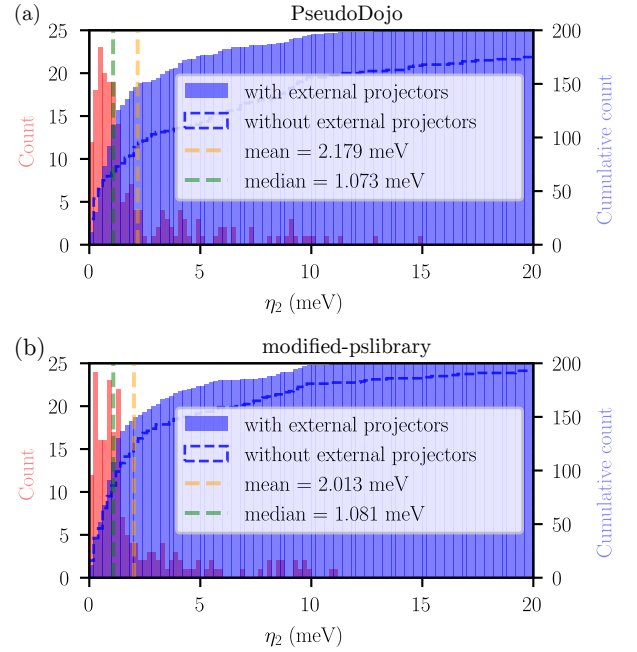


FIG. 2. Band distance η_2 of 200 systems with different pseudopotentials, including SOC effects. Histogram (red) and cumulative histogram (blue) of the band distance η_2 of 200 spin-orbit coupling systems with different pseudopotentials sets: (a) the **PseudoDojo** library, and (b) the **modified-pslibrary** set (see main text). External hydrogenic atomic orbitals are introduced to the projectors to enhance the robustness of the PDWF method, making results obtained with the two pseudopotential libraries qualitatively very similar. As a comparison, the blue dashed lines are the cumulative histogram of η_2 without introducing such external projectors, exhibiting a lower success rate and a strong dependence on the pseudopotential library. The orange (green) vertical line is the mean (median) band distance η_2 of the 200 structures with external projectors; their values are shown in the legend of each panel. All 200 structures can be interpolated with a resulting $\eta_2 \leq 15$ meV for both pseudopotentials libraries, once hydrogenic atomic orbitals are introduced.

tions in the Wannier-interpolated bands near the Fermi level. To identify the source of the error, we examine the projectability of the Bloch states onto the trial PAOs within the first Brillouin zone in Fig. 3(b). The data shows that the projectability remains close to 1 below the Fermi level, but gradually decreases at the Fermi level and above. Notably, already at 2 eV above the Fermi level there are states with essentially zero projectability (the states at the R point). Tracing the k -path from R to M, the projectability increases smoothly from 0, with approximately 0.3 projectability at the k -point ($1/2, 1/2, 1/3$), which is the neighborhood of R on the k -path. However, since we employ the PD + ED algorithm, where ED freezes all bands below $E_F + 2$ eV, the disentanglement process will keep these bands unchanged. Consequently, the almost-zero projectability at R leads to the exclusion of this band during the disentan-

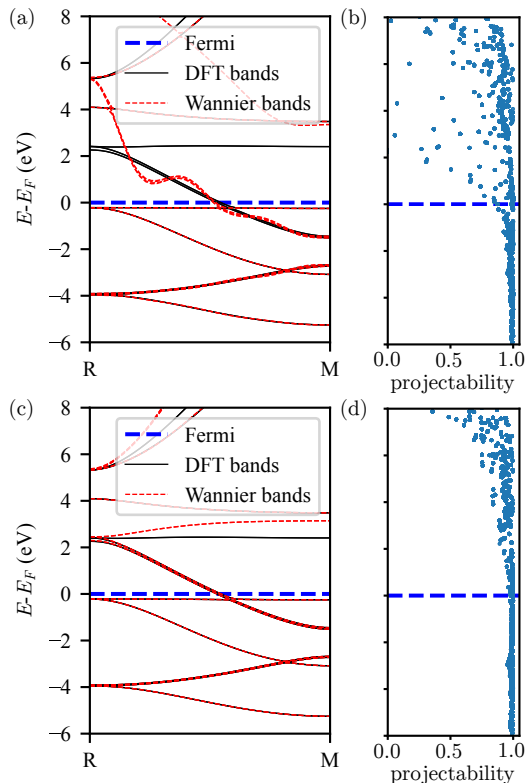


FIG. 3. **Effect of the introduction of additional hydrogenic projectors on the band structure and projectability of AlCo.** (a) DFT bands (black solid lines) compared with Wannier-interpolated bands (red dashed lines) along the R–M path for AlCo without additional hydrogenic projectors, including only the orbitals from the pseudopotential files in the `PseudoDojo` library [38]: $3s$, $3p$, $3d$, $4s$ orbitals for cobalt, and $3s$, $3p$ orbitals for aluminum. (b) Projectability for all k -points for the system of panel (a). The projectability starts to decrease rapidly when the energy is larger than the Fermi level. (c) DFT bands compared with Wannier-interpolated bands when additional hydrogenic $4p$ orbitals are included for cobalt. (d) Projectability for all k -points for the system of panel (c). With the help of hydrogenic AOs, the projectability remains close to one up to a few eV above E_F .

gument, replacing it with a new band constructed from linear combinations of higher-energy bands. As a result, this forces a discontinuity (in reciprocal space) for this band, that is reflected in large oscillations of the resulting Wannier-interpolated bands.

Considering that we wish to maintain the accuracy of the interpolated bands within the $E_F + 2$ eV window, an approach to solve the issue described above for this system is to increase the projectability of bands near the energy window, that can be achieved only by extending the projection space. The most intuitive approach is thus to introduce external projectors to expand the Hilbert space of the projections, thereby enhancing the overall projectability. This was already considered in Ref [21], augmenting the number of projectors for silicon to in-

clude also d states.

There are several approaches possible to obtain external projectors. One approach consists in generating additional projectors using the pseudopotential generation code, and releasing new pseudopotentials. This approach is naturally the most physically accurate and can ensure maximal orthogonality between projectors, while providing the most precise projectability. However, it requires additional manual adaptation for different elements and pseudopotential libraries. Another approach expands the projectors by referencing other libraries, such as complementing missing projectors between `pslibrary` and `PseudoDojo`, or directly obtaining projectors from third-party libraries, like extracting the desired projectors from the PAOs obtained from the `OpenMX` code [21, 44]. However, these often yield projectors defined on different radial coordinates, requiring separate projection calculations or interpolation to align the projectors on a common coordinate system. Moreover, this approach also introduces a higher complexity, depending on several external libraries. Finally, there is no guarantee that the projectors obtained from different libraries are orthogonal to each other. The approach that we will adopt in the following relies instead on adding hydrogenic atomic orbitals. Standard hydrogenic-orbital projectors have been widely used in past applications, and have been effectively applied in HT calculations [19]. Furthermore, since a hydrogenic AO is written using analytical expressions, it can be easily evaluated on the radial coordinates of the original projectors.

As a supplement to the standard hydrogenic approach, we have extended the radial function expressions to accommodate different angular quantum numbers (since the radial part in general depends also on the angular quantum number l , in addition to the principal quantum number n). The various radial functions listed in Table I can cover all the projectors needed for common elements. The shape of these radial functions is controlled by the parameter α . Therefore, in order to define which hydrogenic AOs to use to expand missing projectors, we only need a table containing the minimal required orbitals for each chemical element, together with their corresponding α values. However, compared to projectors generated directly using pseudopotential generation codes, using hydrogenic AO projectors inevitably introduces larger overlaps between AOs and the pseudopotential PAOs, which impacts projectability. While intuitively this is not expected to be an issue for the added projectors, since these are typically needed only to complete the Hilbert space for describing higher-energy bands, we conduct tests to evaluate the effectiveness of this algorithm.

When considering the minimum required orbitals, we follow the principle of including one additional higher AO for elements within the same period. For elements in the n -th period, if $n = 1$, only the $1s$ orbital is considered. For $n = 2$ or 3 , both ns and np orbitals are added to the requirements list. For elements in higher periods, alkali

TABLE I. **Analytical expressions of hydrogenic AOs with different number of radial nodes** ($n_r = n - 1$, where n is the principal quantum number) and angular quantum numbers l . Only the expressions for the values of n_r and l that are needed for covering the missing orbitals in the periodic table are reported.

number of nodes (n_r)	0	1	2
s ($l = 0$)	$2\alpha^{3/2} \exp(-\alpha r)$	$\frac{1}{2\sqrt{2}}\alpha^{3/2}(2 - \alpha r) \exp(-\alpha r/2)$...
p ($l = 1$)	$\frac{1}{2\sqrt{6}}\alpha^{3/2}\alpha r \exp(-\alpha r/2)$	$\frac{4}{81\sqrt{6}}\alpha^{3/2}(6\alpha r - \alpha^2 r^2) \exp(-\alpha r/3)$...
d ($l = 2$)	$\frac{4}{81\sqrt{30}}\alpha^{3/2}\alpha^2 r^2 \exp(-\alpha r/3)$

and alkaline earth metals require ns and $(n-1)d$ orbitals, transition metals need ns , np and $(n-1)d$ orbitals, and elements from the boron group to the noble gases require ns and np . According to these rules, we can list the minimal set of required orbitals for each element, which is also provided explicitly in the Supplementary Table II. Note that some of these orbitals might be redundant (i.e., having almost zero projectability on states below $E_F + 2$ eV). However, with the aim of maximizing the success rate for a fully automated algorithm, we include all of them. An analysis of the projectability of the individual orbitals could be performed as a post-processing step to determine which can be removed, if a minimal Wannier basis set is desired.

We stress that any additional hydrogenic projector should be orthogonal to the existing PAOs from the pseudopotential. In particular, if the pseudopotential PAOs already include an orbital with the same angular quantum number l but smaller principal quantum number n , the additional projector should use a radial function that contains a node. To obtain a table of appropriate α values, we employed two approaches. For projectors with a node in the radial function, we adjust α to ensure that the inner (PAOs) and outer (added hydrogenic AO for which we need to determine α) projectors are orthogonal. For projectors without nodes (i.e., when the pseudopotential does not already include an inner-shell projector with the same l), instead, we derive the α value through fitting of our analytical expressions (Table I) to the PAOs from the **OpenMX** code [44]. Because of the orthogonality condition to the underlying PAOs, the values of α will depend on the chosen pseudopotential library. Values of α for the pseudopotential libraries used in this work can be found in Supplementary Tables III, IV, V and VII.

Despite these precautions, the added orbitals are in general not orthogonal to the PAOs. Therefore, we apply a Gram-Schmidt orthonormalization [45] when external projectors are added. More precisely, we first perform separately two Löwdin orthonormalizations for the PAOs from the pseudopotentials and for the external hydrogenic projectors. Then, we fix the PAOs projectors and perform a further Gram-Schmidt orthonormalization step on the hydrogenic orbitals only, ensuring that the full set (PAOs + additional hydrogenic orbitals) form an orthonormal set. This procedure allows us to faithfully keep the PAOs from pseudopotentials unchanged, while at the same time making sure that external projectors are always orthonormal to pseudopotential PAOs.

Instead, a single Löwdin orthogonalization of all orbitals would distort the PAOs, an undesirable effect since they are accurately describing the system chemistry. For a detailed description of the orthonormalization procedure, see Supplementary Section IV C 3.

The algorithms described above have been implemented and will become available in the next releases of QE [41, 42] (**pw2wannier90.x** code). In addition, we can use the scripts in the **AiiDA-Wannier90-Workflows** repository [46] (folder **dev/projectors**) to extract PAO information from the pseudopotentials and determine the minimal required additional projectors and the corresponding α values, according to the method described above. The script then generates the missing projectors and exports them as a **.dat** file, which serves as an additional input for **pw2wannier90.x**.

Going back to the example of Fig. 3, comparing the PAOs in the **PseudoDojo** with the minimum required AOs, we hypothesized that adding an additional $4p$ AO for cobalt could enhance the overall projectability. The computational results support this hypothesis: after introducing a $4p$ external projector, the minimum projectability near $E_F + 2$ eV increased to approximately 0.8, see Fig. 3(d), which is sufficient to maintain continuity between adjacent k -points using the PD+ED disentanglement approach. The spread of the cobalt WFs decreased from a range of 0.73 – 2.46 \AA^2 to 0.46 – 1.14 \AA^2 , confirming an increased smoothness of the wavefunctions in reciprocal space, thus resulting in more localized WFs and in highly accurate Wannier-interpolated bands (up to 2 eV above E_F), with $\eta_2 = 2.34$ meV, see Fig. 3(c).

The computational results for the 200 materials with SOC, before and after introducing the external projectors, are shown in Fig. 2. The statistical data shows significant improvements. After adding external hydrogenic projectors to PAOs from **PseudoDojo** (**modified-pslibrary**), the mean η_2 decreases from 10.136 (4.597) meV to 2.179 (2.013) meV, and the median η_2 drops from 2.873 (1.411) meV to 1.073 (1.081) meV. Notably, the computational success rate increases from 87.5% (96.5%) to 100% when the **PseudoDojo** (**modified-pslibrary**) is used, with all systems having $\eta_2 \leq 20$ meV. Therefore, by appropriately expanding the projection space, we both improve the robustness of the PDWF approach and strongly mitigate the pseudopotential dependence of the results.

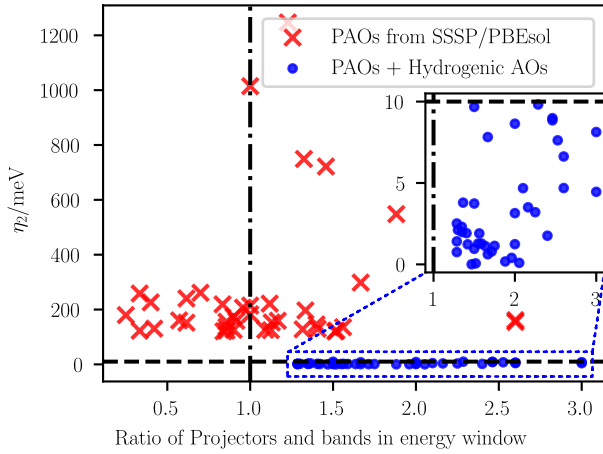


FIG. 4. **Results of recalculating the 40 systems with largest band distance from Ref. [21].** The red crosses are the original data directly from Ref. [21], whose projectors are PAOs from pseudopotentials in SSSP PBEsol Efficiency v1.1. The blue circles are the recalculated data where the same PAOs are complemented by additional hydrogenic AOs. The blue dashed rectangle area (which includes all blue circles) is zoomed in the inset, showing that after adding hydrogenic AOs, all 40 materials have a $\eta_2 \leq 10$ meV, thus demonstrating the effectiveness of our algorithm even in extremely challenging cases.

C. Extended validation in spin-unpolarized systems

In addition to the results on SOC systems mentioned above, we also conducted tests of our extended PDWF method with added hydrogenic projectors on non-SOC systems. As shown in Fig. 5(e), the introduction of external projectors generally reduces the η_2 values, with the mean η_2 decreasing from 4.231 meV to 2.002 meV and the median η_2 dropping from 1.597 meV to 1.153 meV with respect to the values of Ref. [21]. Furthermore, also in this case we achieve a 100% success rate, with $\eta_2 \leq 15$ meV for all materials, and the max distance η_2^{max} also showing a significant reduction.

We further test our extended algorithm on the 40 materials from Ref. [21] that exhibit the largest η_2 among its 21,737 HT results. Each point in Fig. 4 represents a structure, where the x coordinate is the ratio between the number of projectors (i.e., of Wannier functions) and the number of bands within the energy window ($E_F + 2$ eV), while the y coordinate is η_2 . Since each projector can correspond to only one band state, and considering that disentanglement involves a linear combination of several bands, when the number of projectors is less than (or just slightly more than) the number of bands within the energy window, the disentanglement process does not have enough information from the initial projections, possibly resulting in a poor Wannier interpolation. These results clearly indicate that the inaccuracy of the Wannier interpolated bands for many of these materials was due to the lack of a sufficient number of projectors. After adding

external projectors (and enabling the guiding center setting during the Wannierization process), the η_2 for all systems was reduced to below 10 meV (blue circles in Fig. 4). This demonstrates that the additional hydrogenic projectors can significantly enhance the robustness of the Wannier interpolation also in non-SOC systems, even in extremely challenging cases.

To further illustrate how the various components of the extended PDWF method jointly contribute to the overall final robustness of the algorithm, we compare in Fig. 5 the results obtained on the 200-structure set with different projection methods. SOC is not included in these calculations, and the SSSP PBE Efficiency v1.1 pseudopotential library is used, to enable direct comparison with the results of Ref. [21]. Panel (a) of Fig. 5 shows the results of the standard Souza–Marzari–Vanderbilt ED algorithm, using as starting projections the common analytical hydrogenic AOs (as, e.g., defined in the Wannier90 code [47, 48]). The pseudopotential PAOs are used in this case solely to determine the angular character (s , p , d , ...) of the projectors to consider, but no further information is extracted from the pseudopotential projectors. Furthermore, the default values for α and for the projector analytical shapes are employed, as defined in the Wannier90 code. While the approach, that has been widely used in the literature, is able to provide a good Wannier interpolation for over 50% of the systems, it still exhibits a significant number of failures, with a mean η_2 of 64.368 meV and a median η_2 of 7.561 meV.

As discussed earlier, however, the radial part of the hydrogenic orbitals should depend also on the angular quantum number l , meaning that different expressions must be applied for radial functions with s , p , or d angular character (see Table I). Using these corrected radial functions as projectors, combined with optimized values of α (see Supplementary Table IV) obtained by fitting the corresponding PAOs radial functions (and complementing with fitting from OpenMX where PAOs are missing), results in panel (b) of Fig. 5. The success rate significantly increases, and the mean (median) η_2 decreases to 27.478 (5.061) meV, demonstrating that an improved choice of radial functions and α values already enhances the quality of the Wannier interpolation.

Starting from panel (b), two possible directions can be taken to further improve the quality of the Wannier interpolation. The first is to use PDWFs instead of the ED algorithm, see panel (c) of Fig. 5. The mean (median) η_2 further reduces to 12.270 (1.311) meV, demonstrating that the PDWF algorithm can provide a more accurate Wannier interpolation than the standard ED algorithm, even when using the same projectors. (As a note, the large mean η_2 values in panels (a-c) are due to few cases with very large η_2 that are not visible in the histogram as they are outside of the x -axis range.) Alternatively, one can add external hydrogenic AOs to the PAOs, as shown in panel (d) of Fig. 5. The mean (median) η_2 also reduces, with respect to panel (b), to 4.887 (4.225) meV, demonstrating that the addition of external hydrogenic

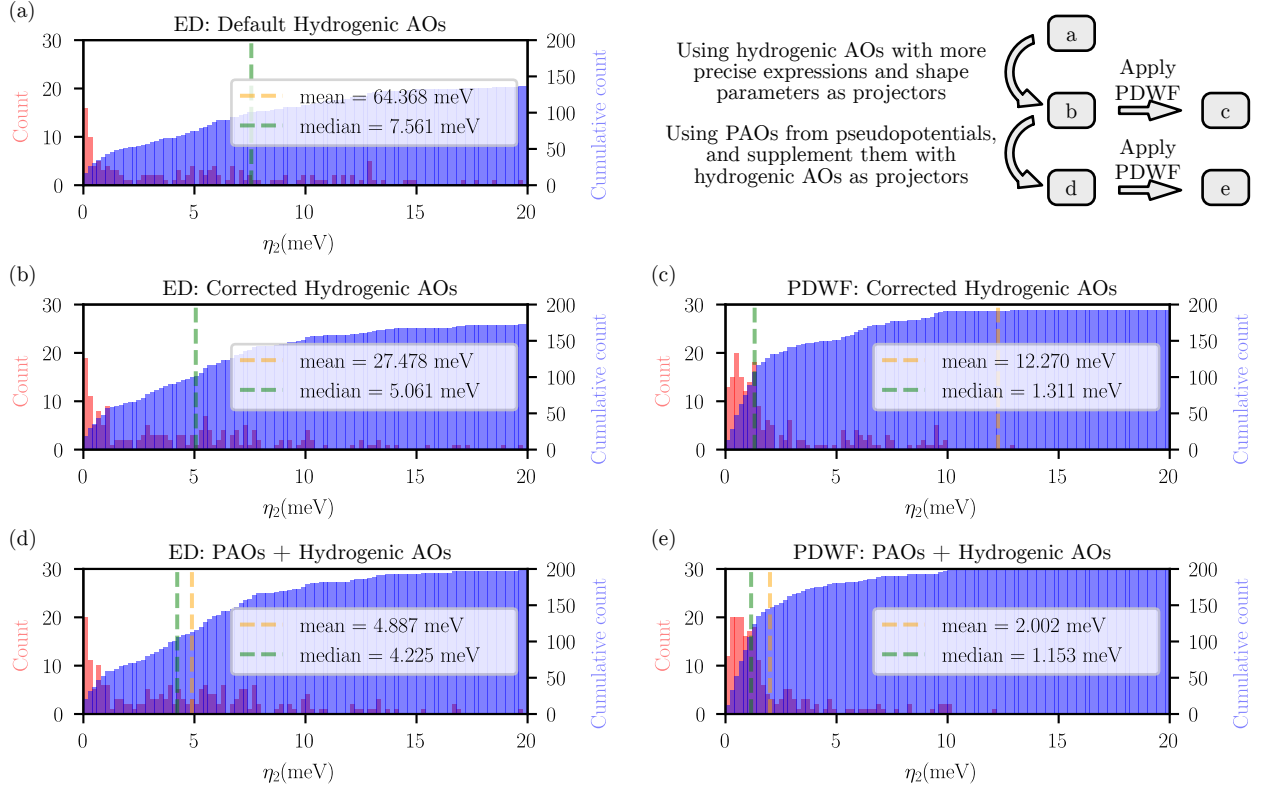


FIG. 5. Summary of the effect of several ingredients of the extended PDWF algorithm on the quality of Wannier interpolation. Histogram (red) and cumulative histogram (blue) of band distance η_2 for our test set of 200 structures, using different algorithms and projectors (all without SOC). All sets of calculations use the same number of projectors and same configurations of semi-core states. All frozen windows were set to $E_F + 2$ eV. (a) ED with the default all-hydrogenic AOs; (b) ED with the corrected all-hydrogenic AOs (see Table I); (c) PDWF with the corrected all-hydrogenic AOs; (d) ED with PAOs and external hydrogenic AOs; and (e) PDWF with PAOs and external hydrogenic AOs. The orange (green) vertical lines are the mean (median) band distance η_2 , whose values are shown in the legend of each panel. The difference and the relation between each set of data are shown in the top right panel. Additional comparisons with further combinations of disentanglement method and starting projectors can be found in Supplementary Section III.

AOs also plays an important role in improving the Wannierization robustness.

Finally, panel (e) of Fig. 5 represents our improved algorithm, combining PDWF and the addition of hydrogenic AOs. The resulting Wannier interpolated bands exhibit the highest quality, with the lowest values for the mean (median) η_2 of 2.002 (1.153) meV, and only such a combination achieves a 100% success rate, with all systems having $\eta_2 \leq 15$ meV.

These results demonstrate that, although hydrogenic AOs are not as physically precise as the projectors from the pseudopotentials, they are still essential as a complement to PAOs when these are not sufficient to cover all states up to $E_F + 2$ eV. The additional advantage is that the present combined method essentially eliminates the dependence of PDWFs on pseudopotentials. In fact, while different pseudopotentials may have different sets of PAOs, discrepancies are minimized by introducing hydrogenic functions to complete the projectors to the same list of orbitals (for a given chemical element), see SI Table II. We also stress that good interpolation quality can

only be achieved if enough PAOs are already included into the pseudopotential (as these capture the detailed chemistry of the material close to the atoms), and we need to possibly add only a few more hydrogenic AOs to recover a large enough projectability for the high-energy bands in the relevant energy range. Indeed, if no PAOs are available at all in the pseudopotentials, only considering hydrogenic AOs is equivalent to panel (b) of Fig. 5, showing that a much lower interpolation quality would be achieved.

The present method thus offers a flexible and straightforward approach to generate the needed additional projectors without requiring to execute and possibly modify the pseudopotential generation codes, making it a practical algorithm for enhancing the performance of PDWFs for high-throughput research.

D. Magnetization

We finally discuss the extension of the PDWF workflows to magnetic systems. In magnetic DFT calculations, one typically distinguishes between a collinear and non-collinear magnetic treatment. The former indicates that the spin can only be polarized along a given quantization axis (e.g., z), which is often appropriate to describe ferromagnetic and collinear antiferromagnetic materials, but can fail to accurately describe the magnetic structure of more complex systems where magnetic moments are not simply parallel or antiparallel, such as non-collinear antiferromagnetic systems or spin spiral states. In a collinear treatment, spinor wavefunctions have one of the two components being identically zero. In QE, the code therefore considers collinear calculations by only storing the non-zero component of the spinor wavefunctions, effectively treating each of the two spin channels as spin-unpolarized calculations, but with a doubled set of k -points (one set for spin up, one for spin down). (Note that this is possible only in the absence of SOC, so that the Hamiltonian does not mix the two spin channels). Consequently, in our workflow design, we choose to separate the spin-up and spin-down calculations, and later merge the band structures after the calculations are completed.

Instead, since formally the treatment of non-collinear spin systems is the same as that of SOC systems, because also in this case the wavefunctions are two-component spinors, the corresponding workflow structure is analogous to that of SOC calculations, with the only additional requirement being a tool to incorporate the magnetic moment as an input. Within the AiiDA-Wannier90-Workflows repository [46] we have developed a new `MagneticStructureData` data plugin for AiiDA (available in the `aiida_wannier90_workflows.data.structure` Python package) that processes magnetic moment structures and organizes input files. In the following two subsections we briefly discuss the results of the verification of our workflows for collinear and non-collinear magnetic systems.

1. Collinear magnetic systems

We performed calculations on 16 relevant magnetic systems, including collinear ferromagnetic body-centered cubic (BCC) iron, collinear antiferromagnetic Mn_2F_4 , and non-collinear antiferromagnetic Li_2IrMn_3 , as well as other magnetic systems primarily composed of Fe, Co, Ni, and Mn elements.

In this set of calculations, the initial magnetic moments in DFT calculations are chosen to have the same magnitude as the z component of the actual 3D magnetic structure. Without applying strain, we allowed the DFT code to converge to the ground-state magnetic moment structure within the framework of a collinear ferromag-

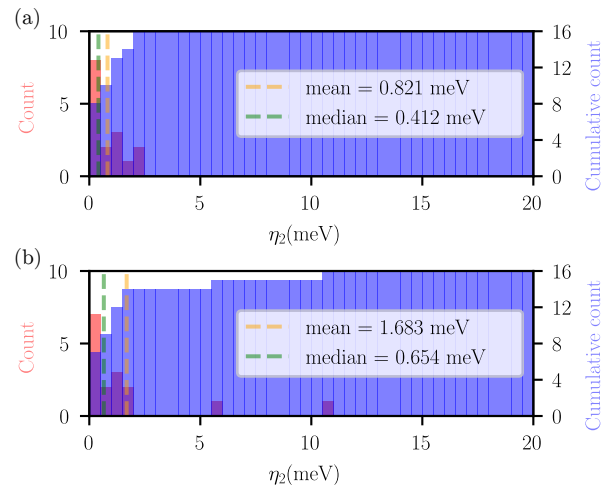


FIG. 6. **Results of the extended PDWF workflows for magnetic (collinear and non-collinear) systems.** Histogram (red) and cumulative histogram (blue) of the band distance η_2 of (a) 16 collinear magnetic systems and (b) 16 non-collinear magnetic systems. The orange (green) vertical lines are the mean (median) band distance η_2 , whose values are shown in the legend of each panel. In both cases, SSSP pseudopotentials and additional external hydrogenic projectors were used to obtain PDWFs.

netic system. Our extended PDWF approach was used to accurately obtain the Wannier functions, incorporating external hydrogenic atomic orbitals into the projectors to enhance robustness, as detailed earlier. The calculated band distances within the energy window of $E_F + 2$ eV are shown in Fig. 6(a). Results on these systems are excellent, with very low mean and median η_2 (both below 1 meV).

2. Non-collinear magnetic systems

Given the complexity of magnetic structures, also in this case we selected only 16 magnetic systems, including both collinear and non-collinear configurations, as well as ferromagnetic and antiferromagnetic systems. The detailed list of materials, with their magnetic configurations, is provided in Supplementary Section V. Using the PDWF algorithm and external hydrogenic AOs, the calculated band distances within the energy window of $E_F + 2$ eV are shown in Fig. 6(b). Also in this case, the MLWFs generated by our extended PDWF method demonstrate an excellent performance in accurately describing electronic structures, with both mean and median η_2 below 2 meV, thus showcasing the effectiveness of our extended PDWF algorithm in treating magnetic systems.

E. Discussion

We present the extension of the PDWF algorithm to collinear and non-collinear magnetic systems, and to systems including SOC. Moreover, we further improve the robustness of the algorithm by defining an automated strategy for incorporating additional external (hydrogenic) projectors when the pseudopotentials do not include sufficient projectors to describe the lowest-energy unoccupied states. Our extended algorithms are fully automated using the AiiDA workflow engine [49–51] and we make our implementation available open-source in the AiiDA-Wannier90-Workflows package [46].

To benchmark the algorithms, we calculate PDWFs for multiple systems (spin-unpolarized, magnetic, and SOC systems) and demonstrate that the present extended PDWF algorithm can reliably and automatically construct MLWF-based tight-binding models for both magnetic and SOC systems. We find that essentially all deviations between Wannier-interpolated bands and DFT bands in earlier (spin-unpolarized) PDWF results [21] can be attributed to the absence of all desirable projectors in the pseudopotentials. This can lead to poor projectability of important low-energy empty states, resulting in less localization of the corresponding Wannier functions and, in turn, in poorer interpolation of the electronic bands. The addition of external hydrogenic projectors can improve significantly the accuracy of PDWFs and minimize the dependence of Wannier interpolation results on the specific set of PAOs defined in the chosen pseudopotentials, achieving in our test set a 100% success rate (defined as an average band distance $\eta_2 \leq 20$ meV; in all systems in our test sets, the band distance remains below 15 meV) when interpolating all bands up to the Fermi level + 2 eV.

Finally, we compare the results of the Wannierization procedure obtained with various types of projectors (only hydrogenic AOs, PAOs, PAOs + external hydrogenic AOs) and we elucidate the key contributions in the extended PDWF algorithm to the overall quality of the Wannier interpolation. The present results underscore how PDWFs can be obtained in a systematic, robust and automated approach, enabling their straightforward and efficient application to several applications ranging from advanced property calculations [10, 52] to high-throughput materials discovery projects [53].

III. METHODS

A. Code implementation

We implemented projections with PAOs and hydrogenic AOs in the `pw2wannier90.x` executable, part of the **QUANTUM ESPRESSO** (QE) [41, 42] package. It can read user-provided custom projector files and calculate the projections of plane wave functions onto the projectors. The implementation supports SOC systems, non-

collinear and collinear magnetic systems, as well as spin-unpolarized systems. The projector files can be generated using a script in the AiiDA-Wannier90-Workflows package [46] based on the rules defined in Sec. II B. Moreover, we implemented a strategy to perform orthogonalization of the projectors by first applying Löwdin orthogonalization [18] separately to the PAOs and to the hydrogenic AOs, and then fixing the PAOs (ensuring that they remain intact) and performing a subsequent Gram–Schmidt orthogonalization [45] of the entire set of projectors, as discussed in the main text.

B. DFT calculations

The DFT calculations are carried out using QE, with various pseudopotential libraries for different systems, as discussed in the main text. Specifically, and unless stated otherwise, for spin-unpolarized systems without SOC we use SSSP PBE Efficiency v1.1 [33]. For SOC systems, we use the **PseudoDoJo** PBE v1.4 (norm-conserving, fully relativistic) library [38] and the **pslibrary** [39, 40] (PAW, fully relativistic) for comparison and validation. The HT calculations are managed with the AiiDA infrastructure [49–51], which submits QE and **Wannier90** [48] calculations to remote clusters, parses and stores the results into a database, while also orchestrating all sequences of simulations and workflows. The automated AiiDA workflows are open-source and hosted on GitHub [46]. To attach magnetic information to the crystal structure, we extend the AiiDA **StructureData** plugin to a new **MagneticStructureData** class, defined as part of the AiiDA-Wannier90-Workflows package. In the future, we plan to replace this custom class with the new **StructureData** class defined in the AiiDA-Atomistic [54] plugin.

ACKNOWLEDGEMENTS

This research was supported by the NCCR MARVEL, a National Centre of Competence in Research, funded by the Swiss National Science Foundation (grant number 205602). YJ acknowledge support by the China Scholarship Council program. JQ acknowledges support by the HORIZON-RIA 2D-PRINTABLE (proposal number: 101135196), and this work has received funding from the Swiss State Secretariat for Education, Research and Innovation (SERI). NP and GP acknowledge support by the Swiss National Science Foundation (SNSF) Project Funding (grant 200021E_206190 “FISH4DIET”). WZ acknowledge support by the National Key Research and Development Program of China (Grant No. 2022YFB4400200), National Natural Science Foundation of China (Grant Nos. T2394474, T2394470), the Beijing Outstanding Young Scientist Program and Tencent Foundation through the XPLOER PRIZE. We acknowledge access to Piz Daint or Alps at the Swiss Na-

tional Supercomputing Centre, Switzerland under MARVEL's share with the project ID mr32. We acknowledge fruitful discussions with Edward Baxter Linscott and Miki Bonacci.

DATA AVAILABILITY

All data generated in this work, as well as scripts to generate relevant plots, are available on the Materials Cloud Archive [55] at <https://doi.org/10.24435/materialscloud:9g-ds> [56]. This entry also includes AiiDA [50] archive files with the full provenance of all simulations and data.

-
- [1] P. Hohenberg and W. Kohn, Inhomogeneous Electron Gas, *Physical Review* **136**, B864 (1964).
 - [2] N. Nagaosa, J. Sinova, S. Onoda, A. H. MacDonald, and N. P. Ong, Anomalous Hall effect, *Reviews of Modern Physics* **82**, 1539 (2010).
 - [3] J. Sinova, S. O. Valenzuela, J. Wunderlich, C. H. Back, and T. Jungwirth, Spin Hall effects, *Reviews of Modern Physics* **87**, 1213 (2015).
 - [4] E. Derunova, Y. Sun, C. Felser, S. S. P. Parkin, B. Yan, and M. N. Ali, Giant intrinsic spin Hall effect in W_3Ta and other A15 superconductors, *Science Advances* **5**, 1 (2019).
 - [5] Y. Yao, L. Kleinman, A. H. MacDonald, J. Sinova, T. Jungwirth, D. Sheng Wang, E. Wang, and Q. Niu, First Principles Calculation of Anomalous Hall Conductivity in Ferromagnetic bcc Fe, *Physical Review Letters* **92**, 4 (2004).
 - [6] G. Y. Guo, S. Murakami, T.-W. Chen, and N. Nagaosa, Intrinsic Spin Hall Effect in Platinum: First-Principles Calculations, *Physical Review Letters* **100**, 096401 (2008).
 - [7] W. Kohn and L. J. Sham, Self-Consistent Equations Including Exchange and Correlation Effects, *Physical Review* **140**, A1133 (1965).
 - [8] N. Marzari, A. A. Mostofi, J. R. Yates, I. Souza, and D. Vanderbilt, Maximally localized Wannier functions: Theory and applications, *Reviews of Modern Physics* **84**, 1419 (2012).
 - [9] N. Marzari and D. Vanderbilt, Maximally localized generalized Wannier functions for composite energy bands, *Physical Review B - Condensed Matter and Materials Physics* **56**, 12847 (1997).
 - [10] A. Marrazzo, S. Beck, E. R. Margine, N. Marzari, A. A. Mostofi, J. Qiao, I. Souza, S. S. Tsirkin, J. R. Yates, and G. Pizzi, Wannier-function software ecosystem for materials simulations, *Reviews of Modern Physics* **96**, 045008 (2024).
 - [11] H. J. Zhang, C. X. Liu, X. L. Qi, X. Y. Deng, X. Dai, S. C. Zhang, and Z. Fang, Electronic structures and surface states of the topological insulator $Bi_{1-x}Sb_x$, *Physical Review B - Condensed Matter and Materials Physics* **80**, 1 (2009).
 - [12] G. Pizzi, D. Volja, B. Kozinsky, M. Fornari, and N. Marzari, Boltzmann: A code for the evaluation of thermoelectric and electronic transport properties with a maximally-localized wannier functions basis, *Computer Physics Communications* **185**, 422 (2014).
 - [13] X. Wang, J. R. Yates, I. Souza, and D. Vanderbilt, Ab initio calculation of the anomalous Hall conductivity by Wannier interpolation, *Physical Review B - Condensed Matter and Materials Physics* **74**, 1 (2006).
 - [14] T. Thonhauser, D. Ceresoli, D. Vanderbilt, and R. Resta, Orbital magnetization in periodic insulators, *Physical Review Letters* **95**, 1 (2005).
 - [15] J. Qiao, J. Zhou, Z. Yuan, and W. Zhao, Calculation of intrinsic spin Hall conductivity by Wannier interpolation, *Physical Review B* **98**, 1 (2018).
 - [16] J. H. Ryoo, C. H. Park, and I. Souza, Computation of intrinsic spin Hall conductivities from first principles using maximally localized Wannier functions, *Physical Review B* **99**, 235113 (2019).
 - [17] I. Souza, N. Marzari, and D. Vanderbilt, Maximally localized Wannier functions for entangled energy bands, *Physical Review B* **65**, 035109 (2001).
 - [18] P.-O. Löwdin, On the Non-Orthogonality Problem Connected with the Use of Atomic Wave Functions in the Theory of Molecules and Crystals, *The Journal of Chemical Physics* **18**, 365 (1950).
 - [19] D. Gresch, Q. Wu, G. W. Winkler, R. Häuselmann, M. Troyer, and A. A. Soluyanov, Automated construction of symmetrized Wannier-like tight-binding models from ab initio calculations, *Physical Review Materials* **2**, 103805 (2018).
 - [20] V. Vitale, G. Pizzi, A. Marrazzo, J. R. Yates, N. Marzari, and A. A. Mostofi, Automated high-throughput Wannierisation, *npj Computational Materials* **6**, 66 (2020).
 - [21] J. Qiao, G. Pizzi, and N. Marzari, Projectability disentanglement for accurate and automated electronic-structure Hamiltonians, *npj Computational Materials* **9**, 208 (2023).
 - [22] J. Qiao, G. Pizzi, and N. Marzari, Automated mixing of maximally localized wannier functions into target manifolds, *npj Computational Materials* **9**, 206 (2023).
 - [23] L. A. Agapito, S. Ismail-Beigi, S. Curtarolo, M. Fornari, and M. B. Nardelli, Accurate tight-binding Hamiltonian matrices from ab initio calculations: Minimal basis sets, *Physical Review B* **93**, 035104 (2016).
 - [24] V. Baltz, A. Manchon, M. Tsoi, T. Moriyama, T. Ono, and Y. Tserkovnyak, Antiferromagnetic spintronics, *Reviews of Modern Physics* **90**, 015005 (2018).
 - [25] D. Xiong, Y. Jiang, K. Shi, A. Du, Y. Yao, Z. Guo, D. Zhu, K. Cao, S. Peng, W. Cai, D. Zhu, and W. Zhao, Antiferromagnetic spintronics: An overview and outlook, *Fundamental Research* **2**, 522 (2022).
 - [26] S. K. Kim, G. S. D. Beach, K.-J. Lee, T. Ono, T. Rasing, and H. Yang, Ferrimagnetic spintronics, *Nature Materials* **21**, 24 (2022).
 - [27] S. Brinker, M. dos Santos Dias, and S. Lounis, Prospecting chiral multisite interactions in prototypical magnetic systems, *Physical Review Research* **2**, 033240 (2020).

- [28] W. S. Ham, A.-M. Pradipto, K. Yakushiji, K. Kim, S. H. Rhim, K. Nakamura, Y. Shiota, S. Kim, and T. Ono, Dzyaloshinskii–Moriya interaction in noncentrosymmetric superlattices, *npj Computational Materials* **7**, 129 (2021).
- [29] N. P. Armitage, E. J. Mele, and A. Vishwanath, Weyl and Dirac semimetals in three-dimensional solids, *Reviews of Modern Physics* **90**, 015001 (2018).
- [30] M. Z. Hasan and C. L. Kane, Colloquium : Topological insulators, *Reviews of Modern Physics* **82**, 3045 (2010).
- [31] H. Zhou, M. dos Santos Dias, Y. Zhang, W. Zhao, and S. Lounis, Kagomerization of transition metal monolayers induced by two-dimensional hexagonal boron nitride, *Nature Communications* **15**, 4854 (2024).
- [32] A. Manchon, H. C. Koo, J. Nitta, S. M. Frolov, and R. A. Duine, New perspectives for Rashba spin-orbit coupling, *Nature Materials* **14**, 871 (2015).
- [33] G. Prandini, A. Marrazzo, I. E. Castelli, N. Mounet, and N. Marzari, Precision and efficiency in solid-state pseudopotential calculations, *npj Computational Materials* **4**, 10.1038/s41524-018-0127-2 (2018).
- [34] M. S. Dresselhaus, G. Dresselhaus, and A. Jorio, *Group Theory* (Springer Berlin Heidelberg, Berlin, Heidelberg, 2008) pp. 1–582.
- [35] D. Xiao, G.-B. Liu, W. Feng, X. Xu, and W. Yao, Coupled spin and valley physics in monolayers of MoS₂ and other group-VI dichalcogenides, *Physical Review Letters* **108**, 196802 (2011).
- [36] P. A. M. Dirac, The quantum theory of the electron, *Proceedings of the Royal Society of London. Series A, Containing Papers of a Mathematical and Physical Character* **117**, 610 (1928).
- [37] F. Bechstedt, *Many-Body Approach to Electronic Excitations*, Springer Series in Solid-State Sciences, Vol. 181 (Springer Berlin Heidelberg, Berlin, Heidelberg, 2015) p. 457.
- [38] M. van Setten, M. Giantomassi, E. Bousquet, M. Verstraete, D. Hamann, X. Gonze, and G.-M. Rignanese, The PseudoDojo: Training and grading a 85 element optimized norm-conserving pseudopotential table, *Computer Physics Communications* **226**, 39 (2018).
- [39] A. Dal Corso, Pseudopotentials periodic table: From H to Pu, *Computational Materials Science* **95**, 337 (2014).
- [40] Suggested pseudopotentials, https://dalcorsi.github.io/pslibrary/PP_list.html, online; accessed 20 January 2025.
- [41] P. Giannozzi, S. Baroni, N. Bonini, M. Calandra, R. Car, C. Cavazzoni, D. Ceresoli, G. L. Chiarotti, M. Cococcioni, I. Dabo, A. Dal Corso, S. De Gironcoli, S. Fabris, G. Fratesi, R. Gebauer, U. Gerstmann, C. Gougoussis, A. Kokalj, M. Lazzeri, L. Martin-Samos, N. Marzari, F. Mauri, R. Mazzarello, S. Paolini, A. Pasquarello, L. Paulatto, C. Sbraccia, S. Scandolo, G. Schlauser, A. P. Seitsonen, A. Smogunov, P. Umari, and R. M. Wentzcovitch, QUANTUM ESPRESSO: A modular and open-source software project for quantum simulations of materials, *Journal of Physics Condensed Matter* **21**, 10.1088/0953-8984/21/39/395502 (2009).
- [42] P. Giannozzi, O. Basergio, P. Bonfà, D. Brunato, R. Car, I. Carnimeo, C. Cavazzoni, S. De Gironcoli, P. Delugas, F. Ferrari Ruffino, A. Ferretti, N. Marzari, I. Timrov, A. Urru, and S. Baroni, QUANTUM ESPRESSO toward the exascale, *Journal of Chemical Physics* **152**, 10.1063/5.0005082 (2020).
- [43] Materials cloud three-dimensional structure database (MC3D), <https://mc3d.materialscloud.org>, online; accessed 20 January 2025.
- [44] T. Ozaki, Variationally optimized atomic orbitals for large-scale electronic structures, *Physical Review B* **67**, 155108 (2003).
- [45] S. J. Leon, Å. Björck, and W. Gander, Gram-Schmidt orthogonalization: 100 years and more, *Numerical Linear Algebra with Applications* **20**, 492 (2013).
- [46] aiida-wannier90-workflows: A collection of advanced automated workflows to compute Wannier functions using AiiDA and the Wannier90 code, <https://github.com/aiidateam/aiida-wannier90-workflows>, online; accessed 22 January 2025.
- [47] A. A. Mostofi, J. R. Yates, Y.-S. Lee, I. Souza, D. Vanderbilt, and N. Marzari, wannier90: A tool for obtaining maximally-localised Wannier functions, *Computer Physics Communications* **178**, 685 (2008).
- [48] G. Pizzi, V. Vitale, R. Arita, S. Blügel, F. Freimuth, G. Géranton, M. Gibertini, D. Gresch, C. Johnson, T. Koretsune, J. Ibañez-Azpiroz, H. Lee, J.-M. Lihm, D. Marchand, A. Marrazzo, Y. Mokrousov, J. I. Mustafa, Y. Nohara, Y. Nomura, L. Paulatto, S. Poncé, T. Ponweiser, J. Qiao, F. Thöle, S. S. Tsirkin, M. Wierzbowska, N. Marzari, D. Vanderbilt, I. Souza, A. A. Mostofi, and J. R. Yates, Wannier90 as a community code: new features and applications, *Journal of Physics: Condensed Matter* **32**, 165902 (2020).
- [49] G. Pizzi, A. Cepellotti, R. Sabatini, N. Marzari, and B. Kozinsky, AiiDA: automated interactive infrastructure and database for computational science, *Computational Materials Science* **111**, 218 (2016).
- [50] S. P. Huber, S. Zoupanos, M. Uhrin, L. Talirz, L. Kahle, R. Häuselmann, D. Gresch, T. Müller, A. V. Yakutovich, C. W. Andersen, F. F. Ramirez, C. S. Adorf, F. Gargiulo, S. Kumbhar, E. Passaro, C. Johnston, A. Merkys, A. Cepellotti, N. Mounet, N. Marzari, B. Kozinsky, and G. Pizzi, AiiDA 1.0, a scalable computational infrastructure for automated reproducible workflows and data provenance, *Scientific Data* **7**, 300 (2020).
- [51] M. Uhrin, S. P. Huber, J. Yu, N. Marzari, and G. Pizzi, Workflows in AiiDA: Engineering a high-throughput, event-based engine for robust and modular computational workflows, *Computational Materials Science* **187**, 110086 (2021).
- [52] Z. Liu, S. Zhang, Z. Fang, H. Weng, and Q. Wu, Combined first-principles and boltzmann transport theory methodology for studying magnetotransport in magnetic materials, *Phys. Rev. Res.* **6**, 043185 (2024).
- [53] M. Bercx, S. Poncé, Y. Zhang, G. Trezza, A. G. Ghezeljehmeidan, L. Bastonero, J. Qiao, F. O. von Rohr, G. Pizzi, E. Chiavazzo, and N. Marzari, Charting the landscape of Bardeen-Cooper-Schrieffer superconductors in experimentally known compounds (2025), arXiv:2503.10943 [cond-mat.supr-con].
- [54] AiiDA-Atomistic: AiiDA plugin for atomistic materials-science simulations, <https://github.com/aiidateam/aiida-atomistic>, online; accessed 27 January 2025.
- [55] L. Talirz, S. Kumbhar, E. Passaro, A. V. Yakutovich, V. Granata, F. Gargiulo, M. Borelli, M. Uhrin, S. P. Huber, S. Zoupanos, C. S. Adorf, C. W. Andersen, O. Schütt, C. A. Pignedoli, D. Passerone, J. VandeVondele, T. C. Schulthess, B. Smit, G. Pizzi, and N. Marzari, Materials cloud, a platform for open computational sci-

- ence, *Scientific Data* **7**, 299 (2020).
- [56] Y. Jiang, J. Qiao, N. Paulish, Z. Weisheng, N. Marzari, and G. Pizzi, Robust Wannierization including magnetization and spin-orbit coupling via projectability disentanglement, 10.24435/materialscloud:9g-ds (2025).

Supplementary Material for: Robust Wannierization including magnetization and spin-orbit coupling via projectability disentanglement

Yuhao Jiang, Junfeng Qiao, Nataliya Paulish, Weisheng Zhao, Nicola Marzari, and Giovanni Pizzi

CONTENTS

I. SOC-weighted band distance	2
II. Band distance after introducing external projectors	3
III. Additional comparisons between approaches for disentanglement and initial projections	3
IV. Orthonormalization strategy	4
A. Diagonalization of a block matrix	4
1. Lemma	4
2. Proof	4
B. Löwdin orthonormalization	4
1. Lemma	4
2. Proof	4
C. Gram–Schmidt orthonormalization	5
1. Classical Gram–Schmidt algorithm	5
2. Modified Gram–Schmidt algorithm	5
3. Modified Gram–Schmidt implemented in <code>pw2wannier90.x</code>	5
V. Magnetic structures	6
VI. Required projectors set for a robust PDWF Wannierization	7
VII. Detailed information on the projectors used in this work	8
References	24

I. SOC-WEIGHTED BAND DISTANCE

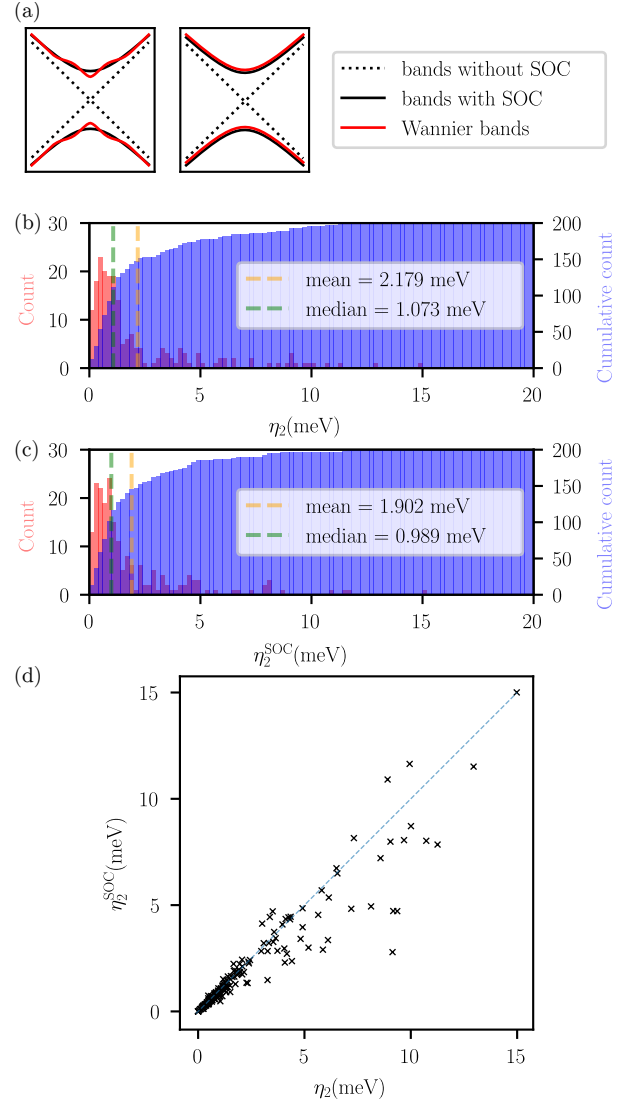
When studying SOC systems, it is expected that the Wannier functions can accurately reproduce the plane wave functions as closely as possible within the SOC-strongly-influenced k -space. In terms of band distance, the accuracy near the SOC-induced band splitting should be maintained at a level comparable to other regions. As shown in an artificial schematics in Supplementary Fig. 1(a), an oscillating interpolated band may have a similar average band distance to that of an interpolated band with a small rigid shift of all bands. However, it is evident that the oscillating energy band corresponds to Wannier functions that are insufficient to accurately describe the system, because of the mismatch of the band splitting and of the band derivatives (which are an important ingredient, e.g., of transport calculations). Therefore, we designed a SOC-weighted band distance metric to emphasize the accuracy of the Wannier-interpolated bands near the SOC-induced splitting.

Similar to the definition of the band distance, we define the SOC-weighted band distance as

$$\eta_{\nu}^{\text{SOC}} = \sqrt{\frac{\sum_{\mathbf{n}\mathbf{k}} \tilde{f}_{\mathbf{n}\mathbf{k}}^{\text{SOC}} (\epsilon_{\mathbf{n}\mathbf{k}}^{\text{DFT}} - \epsilon_{\mathbf{n}\mathbf{k}}^{\text{Wan}})^2}{\sum_{\mathbf{n}\mathbf{k}} \tilde{f}_{\mathbf{n}\mathbf{k}}^{\text{SOC}}}}, \quad (1)$$

where $\tilde{f}_{\mathbf{n}\mathbf{k}}^{\text{SOC}} = \sqrt{\tilde{f}_{\mathbf{n}\mathbf{k}} |\tanh((\epsilon_{\mathbf{n}\mathbf{k}}^{\text{SOC}} - \epsilon_{\mathbf{n}\mathbf{k}}^{\text{noSOC}})/\sigma^{\text{SOC}})|}$, $\tilde{f}_{\mathbf{n}\mathbf{k}}$ being the effective Fermi-Dirac distribution. The \tanh function is used to provide a weight to each band and k -point contribution, dependent on the splitting between the corresponding bands with and without SOC. We selected a σ value of 50 meV, so that for instance a specific state with SOC splitting of 100 meV corresponds to a weight of 0.964, close to 1. In contrast, states without splitting or with very small splitting will have almost no weight.

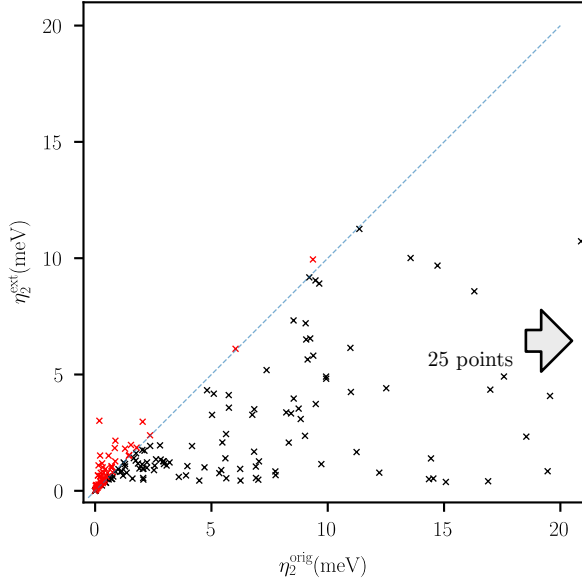
In Supplementary Fig. 1(d), we can observe that the SOC-weighted band distance and the band distance are similar, proving that with our method the interpolation errors when SOC is included are not originating only SOC-specific errors, i.e., from regions where SOC has a large effect, but they are interpolation errors distributed across the BZ. The “standard” band distance can thus be safely used to describe the discrepancy between the Wannier-interpolated bands and the DFT bands also when SOC is included.



SUPPLEMENTARY FIG. 1. (a). Two sketches of Wannier interpolation of bands near a SOC-induced splitting. Note that the two sketches are only schematic representations and do not correspond to the band structure of any real system. While the average band distance in the two sketches is approximately similar, the left figure exhibits significant oscillations near the SOC splitting, which is detrimental for accurately predicting properties dominated by SOC. Histogram (red) and cumulative histogram (blue) of (b) the band distance η_2 and (c) the SOC-weighted band distance η_2^{SOC} . The orange (green) vertical line is the mean (median) band distance, whose value(s) are shown in the legend of each panel. PseudoDojo 0.4 and external hydrogenic projectors were used to perform a PDWF Wannierization. (d) Scatter plot of η_2 vs. η_2^{SOC} , showing that regardless of whether SOC-weighting is applied, the two band distances are approximately the same.

II. BAND DISTANCE AFTER INTRODUCING EXTERNAL PROJECTORS

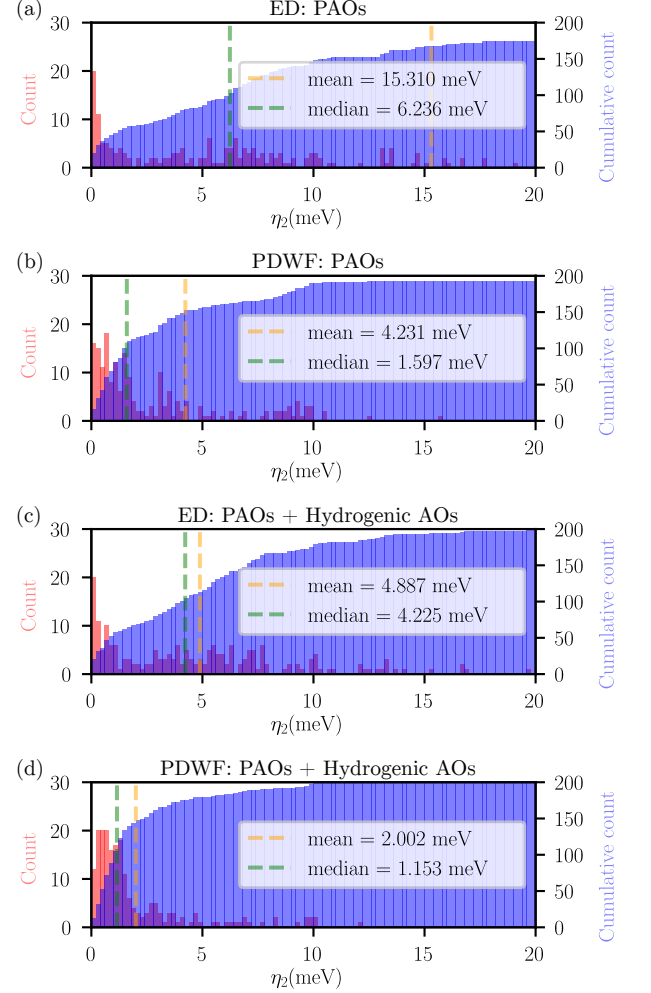
In Sec. IIB of the main paper, we show that adding hydrogenic AOs can improve the performance of Wannier interpolation, especially in increasing the success rate in Supplementary Fig. 2. However, we observed that in regions with already very small band distance, the band distance might slightly increase after adding hydrogenic AOs. This effect is more pronounced when using *PseudoDojo*. To illustrate this, we have plotted the band distance η_2 before and after adding hydrogenic AOs in Supplementary Fig. 2. As a result, in the low- η_2 region, there are instances where the external projector actually increases the band distance (see red crosses in Supplementary Fig. 2). However, since even despite this small increase, the band distance in these systems remains very small, the resulting Wannier interpolation is still of high quality. We thus recommend to introduce by default the addition of external hydrogenic projectors, with the aim of improving the overall quality of Wannier interpolation for any input system in a general way. For systems negatively affected by this, a future workflow could incorporate a final *exclude projector* process to further optimize the results.



SUPPLEMENTARY FIG. 2. Scatter plot of the original band distance (η_2^{orig}) vs. the band distance after adding external projectors (η_2^{ext}) for materials calculated with *PseudoDojo*. The red crosses indicate systems for which the band distance increases after introducing external projectors (i.e., $\eta_2^{\text{ext}} > \eta_2^{\text{orig}}$). We note that for most of these points η_2^{ext} remains < 4 meV, and in general the addition of external projectors has a minimal impact on the overall robustness. 25 structures with large η_2^{orig} but low η_2^{ext} (< 10 meV) are not shown in the figure.

III. ADDITIONAL COMPARISONS BETWEEN APPROACHES FOR DISENTANGLEMENT AND INITIAL PROJECTIONS

We present in Supplementary Fig. 3 the comparison between PAO projectors only and PAO with external hydrogenic AO projectors. At variance with Fig. 5 in the main text, the number of projectors is not the same in all panels. The results of Supplementary Fig. 3 shows that, whether using ED or PDWF, the introduction of external hydrogenic AOs can significantly enhance the robustness and accuracy of the Wannier interpolation.



SUPPLEMENTARY FIG. 3. Histogram (red) and cumulative histogram (blue) of the band distance η_2 for the 200 structures used in Ref. [1] using different algorithms and projectors (without SOC). All frozen windows were set to $E_F + 2$ eV. (a) ED with PAOs; (b) PDWF with PAOs (same as Ref. [1]); (c) ED with PAOs and external hydrogenic AOs; and (d) PDWF with PAOs and external hydrogenic AOs. The orange (green) vertical line is the mean (median) band distance η_2 , whose value(s) are shown in the legend of each panel.

IV. ORTHONORMALIZATION STRATEGY

As discussed in the main text, using a Löwdin orthonormalization on the complete set of the projectors derived from the PAOs in the pseudopotential and from the external hydrogenic AOs is detrimental, as the (chemically accurate) PAOs in the pseudopotential get mixed and thus distorted in order to obtain orthogonality.

Instead, we recommend to apply Löwdin orthonormalization separately to the projectors derived from the PAOs in the pseudopotential and those from the external hydrogenic AOs. Then, we perform Gram–Schmidt orthonormalization on the hydrogenic AOs projectors only, using the PAO projectors as the reference basis. In our implementation, we perform the two Löwdin orthonormalization steps in a single matrix operation, and adopt the modified Gram–Schmidt algorithm for improved numerical precision. This chapter provides a brief overview of the underlying implementation details.

A. Diagonalization of a block matrix

1. Lemma

The eigen decomposition of a block diagonal matrix $A = \begin{bmatrix} A_1 & 0 \\ 0 & A_2 \end{bmatrix} = PDP^{-1}$ can always be written in the form of $P = \begin{bmatrix} P_1 & 0 \\ 0 & P_2 \end{bmatrix}$ and $D = \begin{bmatrix} D_1 \\ D_2 \end{bmatrix}$, where D_1 (D_2) and P_1 (P_2) are the eigenvalues and eigenvectors of A_1 (A_2), respectively, i.e., $A_1 = P_1 D_1 P_1^{-1}$.

2. Proof

Suppose A , A_1 , and A_2 have sizes $n \times n$, $p \times p$, and $q \times q$, respectively, and $p + q = n$. For any eigenvector v of A , $Av = \lambda v$, where $\lambda \in \mathbb{Z}$ and $v \in \mathbb{Z}_n$. If we partition the v into blocks, $v = \begin{bmatrix} v_1 \\ v_2 \end{bmatrix}$ where $v_1 \in \mathbb{Z}_p$ and $v_2 \in \mathbb{Z}_q$, we have

$$\begin{bmatrix} A_1 & 0 \\ 0 & A_2 \end{bmatrix} \begin{bmatrix} v_1 \\ v_2 \end{bmatrix} = \lambda \begin{bmatrix} v_1 \\ v_2 \end{bmatrix} \quad (2)$$

thus

$$\begin{bmatrix} A_1 v_1 \\ A_2 v_2 \end{bmatrix} = \lambda \begin{bmatrix} v_1 \\ v_2 \end{bmatrix}. \quad (3)$$

Therefore, v_1 and v_2 are respectively the eigenvectors of A_1 and A_2 . Now, suppose v is the eigenvector of A and has normal length $\|v\| = 1$, and the v_1 of v is already an eigenvector of A_1 and has normal length $\|v_1\| = 1$, then v_2 of v must be 0, since $\|v\| = \|v_1\| + \|v_2\| \Rightarrow \|v_2\| = 0$.

Therefore, A has in total p eigenvectors $\begin{bmatrix} v_1 \\ 0 \end{bmatrix}$ coming from

A_1 , and q eigenvectors $\begin{bmatrix} 0 \\ v_2 \end{bmatrix}$ coming from A_2 , that are linearly independent between each other. Correspondingly, D has p eigenvalues from A_1 , and q eigenvalues from A_2 . The columns of P are these eigenvectors, and one can always construct a permutation matrix R such that $A = (PR)(R^{-1}DR)(R^{-1}P^{-1})$ and PR has the block diagonal structure. Replacing P by PR , one can always reach the form of $P = \begin{bmatrix} P_1 & 0 \\ 0 & P_2 \end{bmatrix}$ and $D = \begin{bmatrix} D_1 \\ D_2 \end{bmatrix}$, where the columns of P_1 are the eigenvectors v_1 of A_1 , the D_1 are the eigenvalues of A_1 , and similarly for P_2 and D_2 .

B. Löwdin orthonormalization

Suppose we have a complex matrix $A \in \mathbb{Z}_{m \times n}$, the Löwdin orthonormalization converts the columns of A into a set of orthonormal vectors that are as close as possible to the original columns. The columns of A should be linearly independent, thus requiring $m \geq n$.

This is achieved in several steps:

1. compute the overlap matrix $O = A^\dagger A$, which is Hermitian by construction;
2. perform an eigen-decomposition of the overlap matrix, $O = PDP^{-1}$; the eigenvalues $D = \text{diag}(\lambda_1, \dots, \lambda_n)$ are real;
3. take the inverse square root of D , and create a new diagonal matrix $S = \text{diag}(\frac{1}{\sqrt{\lambda_1}}, \dots, \frac{1}{\sqrt{\lambda_n}})$, and a new matrix $U = PSP^{-1}$;
4. the Löwdin orthonormalized matrix is $B = AU$. B is semi-unitary since $B^\dagger B = (PS^\dagger P^\dagger A^\dagger)(APSP^{-1}) = PS^\dagger P^\dagger O P S P^{-1} = PS^\dagger D S P^{-1} = PP^{-1} = 1_{n \times n}$.

1. Lemma

A Löwdin orthonormalization of a block diagonal matrix is equivalent to two separate Löwdin orthonormalizations of the submatrices.

2. Proof

Suppose we have a block diagonal matrix $A = \begin{bmatrix} A_1 & 0 \\ 0 & A_2 \end{bmatrix}$, then the overlap matrix is $O = \begin{bmatrix} A_1^\dagger A_1 & 0 \\ 0 & A_2^\dagger A_2 \end{bmatrix}$. The eigen decomposition of O is $O = PDP^{-1}$. According to Lemma IV A 1, P and D are both block-diagonal and they are composed of the eigenvectors and eigenvalues of A_1 and A_2 . Therefore, the construction of U in step 3 is equivalent to two

separate constructions of U_1 and U_2 for A_1 and A_2 , and the multiplication of U_1 and U_2 is applied separately to A_1 and A_2 . Thus, Lemma IV B 1 holds.

C. Gram–Schmidt orthonormalization

1. Classical Gram–Schmidt algorithm

To transform a $n \times m$ matrix A into a semi-unitary form ($A^\dagger A = I_n$), the Gram–Schmidt algorithm is a commonly used method. The column-wise classical Gram–Schmidt (GS) algorithm can be expressed as

Algorithm 1 Classical Gram–Schmidt algorithm

```

B = A
for j ≤ n do
  for i < j do
    B[:, j] = B[:, j] - ⟨B[:, i], A[:, j]⟩ B[:, i]
  end for
  B[:, j] = B[:, j] / ||B[:, j]||
end for

```

The GS algorithm ensures that each column vector is orthogonal to all preceding columns. As a result, the final matrix B is semi-unitary.

2. Modified Gram–Schmidt algorithm

Since we implement the GS algorithm through computer code, modern computing commonly employs the modified GS algorithm, which has lower numerical errors. The algorithm principle is as follows:

Algorithm 2 Modified Gram–Schmidt algorithm

```

B = A
for j ≤ n do
  for i < j do
    B[:, j] = B[:, j] - ⟨B[:, i], B[:, j]⟩ B[:, i]
  end for
  B[:, j] = B[:, j] / ||B[:, j]||
end for

```

Mathematically, the two algorithms are equivalent, but the modified GS algorithm exhibits better numerical orthogonality.

3. Modified Gram–Schmidt implemented in *pw2wannier90.x*

All discussions in this section are based on the case of ultrasoft pseudopotentials (USPP). Namely, an Hermitian overlap operator \hat{S} is required to achieve $\langle \psi | \hat{S} | \psi \rangle = 1$. For non-USPP cases, one can simply take $\hat{S} = \hat{I}$.

We have $n = n_P + n_H$ projectors, of which n_P are from Pseudo Atomic Orbitals (PAOs) and n_H from external hydrogenic AOs. The real projector matrix is

$$A = \begin{bmatrix} A_P & A_H \end{bmatrix}$$

and the overlap matrix is

$$O = A^\dagger \hat{S} A = \begin{bmatrix} A_P^\dagger \hat{S} A_P & A_H^\dagger \hat{S} A_P \\ A_P^\dagger \hat{S} A_H & A_H^\dagger \hat{S} A_H \end{bmatrix},$$

where A_P and A_H are the projector matrices of PAOs and hydrogenic AOs respectively. However, we do not use the conventional Löwdin orthonormalization on the full set of n projectors, as the procedure would also change the PAOs. So we first set the $A_H^\dagger \hat{S} A_P$ and $A_P^\dagger \hat{S} A_H$ to 0 in the overlap matrix, and then perform a Löwdin orthonormalization, so that the matrix we orthonormalize can actually be written as

$$A = \begin{bmatrix} A_P & 0 \\ 0 & A_H \end{bmatrix}.$$

According to Lemma IV B 1, the orthonormalization is equivalent to orthonormalizing the two sets of projectors separately.

When the matrix is written in the real projector form, it becomes

$$A = \begin{bmatrix} O_P^{-1/2} A_P & O_H^{-1/2} A_H \end{bmatrix}$$

and

$$SA = \begin{bmatrix} O_P^{-1/2} S A_P & O_H^{-1/2} S A_H \end{bmatrix}.$$

The off-diagonal part of the overlap matrix $\langle S, SA \rangle$ is not 0. So, an extra GS process is required to orthonormalize the projector matrix, while still keeping the PAOs unchanged. We therefore consider the projectors from PAOs frozen, and thus we can calculate the matrix by

Algorithm 3 Practical algorithm in *pw2wannier90.x*

```

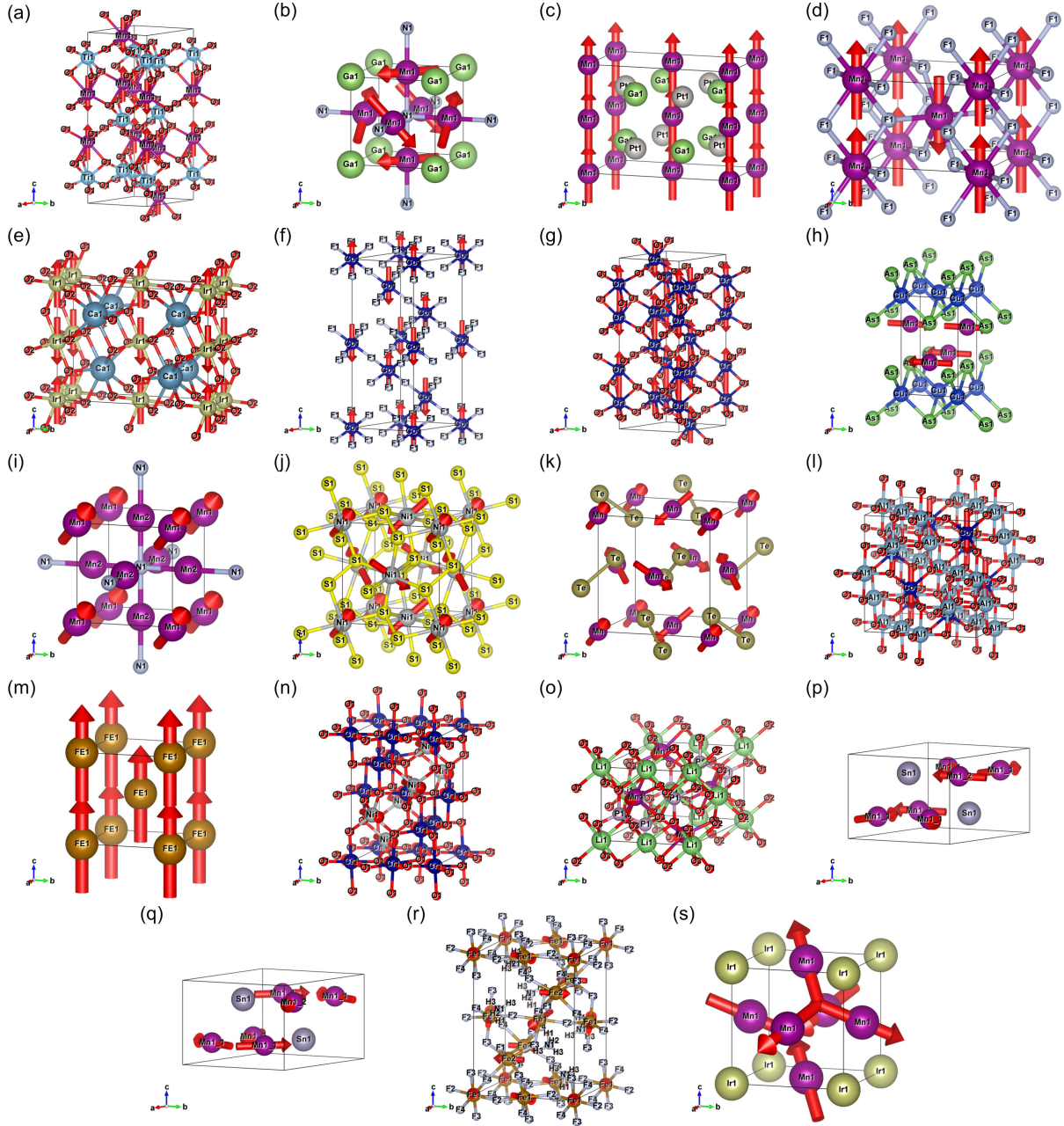
B = A
SB = SA
for projector j not in frozen projectors do
  for projector i in frozen projectors do
    B[:, j] = B[:, j] - ⟨B[:, i], SB[:, j]⟩ B[:, i]
    SB[:, j] = SB[:, j] - ⟨B[:, i], SB[:, j]⟩ SB[:, i]
  end for
  SB[:, j] = SB[:, j] / ⟨B[:, j], SB[:, j]⟩
  set projector j frozen
end for

```

thus obtaining the final projection matrix SB .

V. MAGNETIC STRUCTURES

With the goal of selecting a representative set of materials with a diversity of magnetic moment configurations, we selected several small- to medium-scale collinear and non-collinear magnetic structures from the MAGNDATA database [2]. These are graphically shown in Supplementary Fig. 4 and listed in Supplementary Table I.



SUPPLEMENTARY FIG. 4. Visualization of the magnetic crystal structures used in collinear and non-collinear spin calculations, also listed in Supplementary Table I: (a) $\text{Mn}_2\text{O}_6\text{Ti}_2$, (b) GaMn_3N , (c) $\text{Ga}_2\text{Mn}_2\text{Pt}_2$, (d) F_4Mn_2 , (e) $\text{Ca}_2\text{Ir}_2\text{O}_6$, (f) Co_2F_6 , (g) Cr_4O_6 , (h) $\text{As}_2\text{Cu}_2\text{Mn}_2$, (i) Mn_4N , (j) Ni_4S_8 , (k) Mn_4Te_8 , (l) $\text{Al}_4\text{Co}_2\text{O}_8$, (m) Fe , (n) $\text{Cr}_4\text{Ni}_2\text{O}_8$, (o) $\text{Li}_4\text{Mn}_4\text{O}_{16}\text{P}_4$, (p) Mn_6Sn_2 , (q) Mn_6Sn_2 , (r) $\text{F}_{24}\text{Fe}_8\text{H}_{16}\text{N}_4$, (s) IrMn_3 . Magnetic moments are represented by red arrows.

SUPPLEMENTARY TABLE I. Magnetic structures used in collinear and non-collinear spin calculations.

Label	Formula	Collinear calculation	Non-collinear calculation
a	Mn ₂ O ₆ Ti ₂	✓	✓
b	GaMn ₃ N	✓	
c	Ga ₂ Mn ₂ Pt ₂	✓	✓
d	F ₄ Mn ₂	✓	✓
e	Ca ₂ Ir ₂ O ₆	✓	✓
f	Co ₂ F ₆	✓	✓
g	Cr ₄ O ₆	✓	✓
h	As ₂ Cu ₂ Mn ₂	✓	✓
i	Mn ₄ N	✓	✓
j	Ni ₄ S ₈	✓	✓
k	Mn ₄ Te ₈	✓	✓
l	Al ₄ Co ₂ O ₈	✓	✓
m	Fe	✓	✓
n	Cr ₄ Ni ₂ O ₈		✓
o	Li ₄ Mn ₄ O ₁₆ P ₄	✓	✓
p	Mn ₆ Sn ₂		✓
q	Mn ₆ Sn ₂		✓
r	F ₂₄ Fe ₈ H ₁₆ N ₄	✓	
s	IrMn ₃	✓	

VI. REQUIRED PROJECTORS SET FOR A ROBUST PDWF WANNIERIZATION

In the main text, we employed a relatively aggressive strategy (see Section IIB in the main text for detailed rules) to define a set of projectors that stabilize most PDWFs. These orbitals are listed in Supplementary Table II. We stress that, however, in practical applications this setting may result in an excessive number of projectors for certain structures. Thus, users are encouraged to select an appropriate projector set based on the specific system of interest.

SUPPLEMENTARY TABLE II: Required orbitals for a robust PDWF Wannierization.

<i>Z</i>	Element	Required orbitals
1	H	1 <i>s</i>
2	He	1 <i>s</i>
3	Li	2 <i>s</i> 2 <i>p</i>
4	Be	2 <i>s</i> 2 <i>p</i>
5	B	2 <i>s</i> 2 <i>p</i>
6	C	2 <i>s</i> 2 <i>p</i>
7	N	2 <i>s</i> 2 <i>p</i>
8	O	2 <i>s</i> 2 <i>p</i>
9	F	2 <i>s</i> 2 <i>p</i>
10	Ne	2 <i>s</i> 2 <i>p</i>
11	Na	3 <i>s</i> 3 <i>p</i>
12	Mg	3 <i>s</i> 3 <i>p</i>
13	Al	3 <i>s</i> 3 <i>p</i>
14	Si	3 <i>s</i> 3 <i>p</i>
15	P	3 <i>s</i> 3 <i>p</i>
16	S	3 <i>s</i> 3 <i>p</i>
17	Cl	3 <i>s</i> 3 <i>p</i>
18	Ar	3 <i>s</i> 3 <i>p</i>
19	K	4 <i>s</i> 3 <i>d</i>
20	Ca	4 <i>s</i> 3 <i>d</i>
21	Sc	4 <i>s</i> 4 <i>p</i> 3 <i>d</i>
22	Ti	4 <i>s</i> 4 <i>p</i> 3 <i>d</i>
23	V	4 <i>s</i> 4 <i>p</i> 3 <i>d</i>
24	Cr	4 <i>s</i> 4 <i>p</i> 3 <i>d</i>
25	Mn	4 <i>s</i> 4 <i>p</i> 3 <i>d</i>
26	Fe	4 <i>s</i> 4 <i>p</i> 3 <i>d</i>
27	Co	4 <i>s</i> 4 <i>p</i> 3 <i>d</i>
28	Ni	4 <i>s</i> 4 <i>p</i> 3 <i>d</i>
29	Cu	4 <i>s</i> 4 <i>p</i> 3 <i>d</i>
30	Zn	4 <i>s</i> 4 <i>p</i> 3 <i>d</i>
31	Ga	4 <i>s</i> 4 <i>p</i>
32	Ge	4 <i>s</i> 4 <i>p</i>
33	As	4 <i>s</i> 4 <i>p</i>
34	Se	4 <i>s</i> 4 <i>p</i>
35	Br	4 <i>s</i> 4 <i>p</i>
36	Kr	4 <i>s</i> 4 <i>p</i>
37	Rb	5 <i>s</i> 4 <i>d</i>
38	Sr	5 <i>s</i> 4 <i>d</i>
39	Y	5 <i>s</i> 5 <i>p</i> 4 <i>d</i>
40	Zr	5 <i>s</i> 5 <i>p</i> 4 <i>d</i>
41	Nb	5 <i>s</i> 5 <i>p</i> 4 <i>d</i>
42	Mo	5 <i>s</i> 5 <i>p</i> 4 <i>d</i>
43	Tc	5 <i>s</i> 5 <i>p</i> 4 <i>d</i>
44	Ru	5 <i>s</i> 5 <i>p</i> 4 <i>d</i>
45	Rh	5 <i>s</i> 5 <i>p</i> 4 <i>d</i>
46	Pd	5 <i>s</i> 5 <i>p</i> 4 <i>d</i>

<i>Z</i>	Element	Required orbitals
47	Ag	5 <i>s</i> 5 <i>p</i> 4 <i>d</i>
48	Cd	5 <i>s</i> 5 <i>p</i> 4 <i>d</i>
49	In	5 <i>s</i> 5 <i>p</i>
50	Sn	5 <i>s</i> 5 <i>p</i>
51	Sb	5 <i>s</i> 5 <i>p</i>
52	Te	5 <i>s</i> 5 <i>p</i>
53	I	5 <i>s</i> 5 <i>p</i>
54	Xe	5 <i>s</i> 5 <i>p</i>
55	Cs	6 <i>s</i> 5 <i>d</i>
56	Ba	6 <i>s</i> 5 <i>d</i>
72	Hf	6 <i>s</i> 6 <i>p</i> 5 <i>d</i>
73	Ta	6 <i>s</i> 6 <i>p</i> 5 <i>d</i>
74	W	6 <i>s</i> 6 <i>p</i> 5 <i>d</i>
75	Re	6 <i>s</i> 6 <i>p</i> 5 <i>d</i>
76	Os	6 <i>s</i> 6 <i>p</i> 5 <i>d</i>
77	Ir	6 <i>s</i> 6 <i>p</i> 5 <i>d</i>
78	Pt	6 <i>s</i> 6 <i>p</i> 5 <i>d</i>
79	Au	6 <i>s</i> 6 <i>p</i> 5 <i>d</i>
80	Hg	6 <i>s</i> 6 <i>p</i> 5 <i>d</i>
81	Tl	6 <i>s</i> 6 <i>p</i>
82	Pb	6 <i>s</i> 6 <i>p</i>
83	Bi	6 <i>s</i> 6 <i>p</i>
84	Po	6 <i>s</i> 6 <i>p</i>
85	At	6 <i>s</i> 6 <i>p</i>
86	Rn	6 <i>s</i> 6 <i>p</i>

VII. DETAILED INFORMATION ON THE PROJECTORS USED IN THIS WORK

Based on the radial expression of hydrogenic AOs (see Table I in main text for details), we obtained external projectors using different approaches, including orthonormalization fitting (detailed see Section IIB in the main text) and all-hydrogenic fitting, which is the method to generate the projectors for “corrected hydrogenic AOs”. The latter involves fitting the electron in the innermost shell to the pseudopotential PAOs while applying orthogonalization methods as much as possible to assign α to outer hydrogenic AOs. For missing AOs without inner shells, where therefore there is no orthogonality condition for the radial part to satisfy, we consider PAOs from OpenMX [3] and fit them accordingly to obtain the α values.

The values for the various pseudopotential libraries used in the main text, as well as using different orthogonalization fitting schemes, are reported in Supplementary Tables III, IV and V. The choice of α for the **modified-pslibrary** set (whose choice of pseudopotentials is reported in Supplementary Table VI) is reported in Supplementary Table VII.

In the Source column of the tables, “Pseudopotential” means that the orbital is simply taken from the PAO from the pseudopotential file, “Orthogonalization” means that the value is obtained by achieving orthogonality with the underlying PAO with same angular momentum l , while “OpenMX Fitting” or “Pseudopotential Fitting” indicate that the value has been obtained by fitting the corresponding atomic orbital from the OpenMX dataset [3] or from the pseudopotential PAOs. α values are in unit of bohr^{-1} .

Finally, to facilitate users in generating external projectors for other pseudopotential libraries, we provide in Supplementary Table VIII the α values for all hydrogenic AOs that we fitted in this work using **OpenMX**. This table allows users to use data directly from the table for projector generation. The recommended procedure to determine the α values for a new pseudopotential library is the following. First, use our script in the AiiDA-Wannier90-Workflows repository to generate external hydrogenic AOs based on the pseudopotential PAOs. Then, for missing projectors with nodes, employ orthogonalization fitting with the inner PAOs from pseudopotential to ensure greater accuracy. Finally, for any remaining projectors without nodes, use the value from Supplementary Table VIII.

SUPPLEMENTARY TABLE III: Values of α and minimal set of orbitals for the pseudopotentials of the SSSP PBE Efficiency v1.1 with orthonormalization fitting.

Z	Element	Orbital l	Source	$\alpha(\text{bohr}^{-1})$
1	H	1s	0 Pseudopotential	—
2	He	1s	0 Pseudopotential	—
3	Li	1s	0 Pseudopotential	—
		2s	0 Pseudopotential	—
		2p	1 Pseudopotential	—
4	Be	1s	0 Pseudopotential	—
		2s	0 Pseudopotential	—
		2p	1 Pseudopotential	—
5	B	2s	0 Pseudopotential	—
		2p	1 Pseudopotential	—
6	C	2s	0 Pseudopotential	—
		2p	1 Pseudopotential	—
7	N	2s	0 Pseudopotential	—
		2p	1 Pseudopotential	—
8	O	2s	0 Pseudopotential	—
		2p	1 Pseudopotential	—
9	F	2s	0 Pseudopotential	—
		2p	1 Pseudopotential	—
10	Ne	2s	0 Pseudopotential	—
		2p	1 Pseudopotential	—
		3s	0 Pseudopotential	—
11	Na	2p	1 Pseudopotential	—
		3p	1 Orthogonalization	4.500
12	Mg	3s	0 Pseudopotential	—
		3p	1 Pseudopotential	—
13	Al	3s	0 Pseudopotential	—
		3p	1 Pseudopotential	—
14	Si	3s	0 Pseudopotential	—
		3p	1 Pseudopotential	—
15	P	3s	0 Pseudopotential	—
		3p	1 Pseudopotential	—
16	S	3s	0 Pseudopotential	—
		3p	1 Pseudopotential	—
17	Cl	3s	0 Pseudopotential	—
		3p	1 Pseudopotential	—
18	Ar	3s	0 Pseudopotential	—
		3p	1 Pseudopotential	—
		4s	0 Pseudopotential	—
		4p	1 Pseudopotential	—
19	K	3p	1 Pseudopotential	—
		4p	1 Pseudopotential	—
		3d	2 OpenMX Fitting	2.727
		3s	0 Pseudopotential	—
20	Ca	4s	0 Pseudopotential	—
		3p	1 Pseudopotential	—
		3d	2 Pseudopotential	—
		3s	0 Pseudopotential	—
21	Sc	4s	0 Pseudopotential	—
		3p	1 Pseudopotential	—
		3d	2 Pseudopotential	—
		4p	1 Orthogonalization	4.200
22	Ti	3s	0 Pseudopotential	—
		4s	0 Pseudopotential	—
		3p	1 Pseudopotential	—
		3d	2 Pseudopotential	—
		4p	1 Orthogonalization	4.400

Z	Element	Orbital l	Source	$\alpha(\text{bohr}^{-1})$
23	V	3s	0 Pseudopotential	—
		4s	0 Pseudopotential	—
		3p	1 Pseudopotential	—
		3d	2 Pseudopotential	—
		4p	1 Orthogonalization	4.600
24	Cr	3s	0 Pseudopotential	—
		4s	0 Pseudopotential	—
		3p	1 Pseudopotential	—
		3d	2 Pseudopotential	—
		4p	1 Orthogonalization	4.900
25	Mn	3s	0 Pseudopotential	—
		4s	0 Pseudopotential	—
		3p	1 Pseudopotential	—
		4p	1 Pseudopotential	—
		3d	2 Pseudopotential	—
26	Fe	3s	0 Pseudopotential	—
		4s	0 Pseudopotential	—
		3p	1 Pseudopotential	—
		4p	1 Pseudopotential	—
		3d	2 Pseudopotential	—
27	Co	3s	0 Pseudopotential	—
		4s	0 Pseudopotential	—
		3p	1 Pseudopotential	—
		4p	1 Pseudopotential	—
		3d	2 Pseudopotential	—
28	Ni	3s	0 Pseudopotential	—
		4s	0 Pseudopotential	—
		3p	1 Pseudopotential	—
		4p	1 Pseudopotential	—
		3d	2 Pseudopotential	—
29	Cu	3s	0 Pseudopotential	—
		4s	0 Pseudopotential	—
		3p	1 Pseudopotential	—
		4p	1 Pseudopotential	—
		3d	2 Pseudopotential	—
30	Zn	3s	0 Pseudopotential	—
		4s	0 Pseudopotential	—
		3p	1 Pseudopotential	—
		4p	1 Pseudopotential	—
		3d	2 Pseudopotential	—
31	Ga	4s	0 Pseudopotential	—
		4p	1 Pseudopotential	—
		3d	2 Pseudopotential	—
32	Ge	4s	0 Pseudopotential	—
		4p	1 Pseudopotential	—
		3d	2 Pseudopotential	—
33	As	4s	0 Pseudopotential	—
		4p	1 Pseudopotential	—
34	Se	4s	0 Pseudopotential	—
		4p	1 Pseudopotential	—
35	Br	4s	0 Pseudopotential	—
		4p	1 Pseudopotential	—
36	Kr	4s	0 Pseudopotential	—
		4p	1 Pseudopotential	—
		4s	0 Pseudopotential	—
37	Rb	5s	0 Pseudopotential	—
		4p	1 Pseudopotential	—
		4d	2 OpenMX Fitting	2.197

Z	Element	Orbital l	Source	$\alpha(\text{bohr}^{-1})$
38	Sr	4s	0	Pseudopotential —
		5s	0	Pseudopotential —
		4p	1	Pseudopotential —
		5p	1	Pseudopotential —
		4d	2	Pseudopotential —
39	Y	4s	0	Pseudopotential —
		5s	0	Pseudopotential —
		4p	1	Pseudopotential —
		5p	1	Pseudopotential —
		4d	2	Pseudopotential —
40	Zr	4s	0	Pseudopotential —
		5s	0	Pseudopotential —
		4p	1	Pseudopotential —
		5p	1	Pseudopotential —
		4d	2	Pseudopotential —
41	Nb	4s	0	Pseudopotential —
		5s	0	Pseudopotential —
		4p	1	Pseudopotential —
		4d	2	Pseudopotential —
		5p	1	Orthogonalization 4.100
42	Mo	4s	0	Pseudopotential —
		5s	0	Pseudopotential —
		4p	1	Pseudopotential —
		4d	2	Pseudopotential —
		5p	1	Orthogonalization 4.300
43	Tc	4s	0	Pseudopotential —
		5s	0	Pseudopotential —
		4p	1	Pseudopotential —
		4d	2	Pseudopotential —
		5p	1	Orthogonalization 4.400
44	Ru	4s	0	Pseudopotential —
		5s	0	Pseudopotential —
		4p	1	Pseudopotential —
		4d	2	Pseudopotential —
		5p	1	Orthogonalization 4.600
45	Rh	4s	0	Pseudopotential —
		5s	0	Pseudopotential —
		4p	1	Pseudopotential —
		4d	2	Pseudopotential —
		5p	1	Orthogonalization 4.800
46	Pd	4s	0	Pseudopotential —
		5s	0	Pseudopotential —
		4p	1	Pseudopotential —
		4d	2	Pseudopotential —
		5p	1	Orthogonalization 5.000
47	Ag	4s	0	Pseudopotential —
		5s	0	Pseudopotential —
		4p	1	Pseudopotential —
		4d	2	Pseudopotential —
		5p	1	Orthogonalization 5.100
48	Cd	5s	0	Pseudopotential —
		5p	1	Pseudopotential —
		4d	2	Pseudopotential —
49	In	5s	0	Pseudopotential —
		5p	1	Pseudopotential —
		4d	2	Pseudopotential —
50	Sn	5s	0	Pseudopotential —
		5p	1	Pseudopotential —
		4d	2	Pseudopotential —
51	Sb	5s	0	Pseudopotential —
		5p	1	Pseudopotential —
		4d	2	Pseudopotential —

Z	Element	Orbital l	Source	$\alpha(\text{bohr}^{-1})$
52	Te	5s	0	Pseudopotential —
		5p	1	Pseudopotential —
53	I	5s	0	Pseudopotential —
		5p	1	Pseudopotential —
54	Xe	5s	0	Pseudopotential —
		5p	1	Pseudopotential —
		4d	2	Pseudopotential —
55	Cs	5s	0	Pseudopotential —
		6s	0	Pseudopotential —
		5p	1	Pseudopotential —
		6p	1	Pseudopotential —
56	Ba	5d	2	Pseudopotential —
		5s	0	Pseudopotential —
		6s	0	Pseudopotential —
		5p	1	Pseudopotential —
72	Hf	5d	2	OpenMX Fitting 3.039
		5s	0	Pseudopotential —
		6s	0	Pseudopotential —
		5p	1	Pseudopotential —
		5d	2	Pseudopotential —
73	Ta	6p	1	Orthogonalization 3.900
		5s	0	Pseudopotential —
		6s	0	Pseudopotential —
		5p	1	Pseudopotential —
		6p	1	Pseudopotential —
74	W	5d	2	Pseudopotential —
		5s	0	Pseudopotential —
		6s	0	Pseudopotential —
		5p	1	Pseudopotential —
		6p	1	Pseudopotential —
75	Re	5d	2	Pseudopotential —
		5s	0	Pseudopotential —
		6s	0	Pseudopotential —
		5p	1	Pseudopotential —
		6p	1	Pseudopotential —
76	Os	5d	2	Pseudopotential —
		5s	0	Pseudopotential —
		6s	0	Pseudopotential —
		5p	1	Pseudopotential —
		6p	1	Pseudopotential —
77	Ir	5d	2	Pseudopotential —
		6s	0	Pseudopotential —
		5p	1	Pseudopotential —
		6p	1	Pseudopotential —
		5d	2	Pseudopotential —
78	Pt	6s	0	Pseudopotential —
		5p	1	Pseudopotential —
		6p	1	Pseudopotential —
		5d	2	Pseudopotential —
		5s	0	Pseudopotential —
79	Au	6s	0	Pseudopotential —
		5p	1	Pseudopotential —
		5d	2	Pseudopotential —
		6p	1	Orthogonalization 5.000
		5s	0	Pseudopotential —
80	Hg	6s	0	Pseudopotential —
		5p	1	Pseudopotential —
		5d	2	Pseudopotential —
		6p	1	Orthogonalization 5.100
81	Tl	6s	0	Pseudopotential —
		6p	1	Pseudopotential —
		5d	2	Pseudopotential —

Z	Element	Orbital l	Source	$\alpha(\text{bohr}^{-1})$
82	Pb	$6s$	0	Pseudopotential —
		$6p$	1	Pseudopotential —
		$5d$	2	Pseudopotential —
83	Bi	$6s$	0	Pseudopotential —
		$6p$	1	Pseudopotential —
		$5d$	2	Pseudopotential —
84	Po	$6s$	0	Pseudopotential —
		$6p$	1	Pseudopotential —
		$5d$	2	Pseudopotential —
86	Rn	$6s$	0	Pseudopotential —
		$6p$	1	Pseudopotential —
		$5d$	2	Pseudopotential —

SUPPLEMENTARY TABLE IV: Values of α and minimal set of orbitals for the pseudopotentials of the SSSP PBE Efficiency v1.1 with all-hydrogenic fitting.

Z	Element	Orbital l	Source	$\alpha(\text{bohr}^{-1})$
1	H	$1s$	0	Pseudopotential Fitting 0.910
2	He	$1s$	0	Pseudopotential Fitting 1.522
		$1s$	0	Pseudopotential Fitting 1.252
3	Li	$2s$	0	Orthogonalization 1.252
		$2p$	1	Pseudopotential Fitting 1.205
		$1s$	0	Pseudopotential Fitting 0.702
4	Be	$2s$	0	Orthogonalization 0.702
		$2p$	1	Pseudopotential Fitting 1.612
		$2s$	0	Pseudopotential Fitting 0.614
5	B	$2p$	1	Pseudopotential Fitting 2.283
		$2s$	0	Pseudopotential Fitting 0.863
6	C	$2p$	1	Pseudopotential Fitting 2.834
		$2s$	0	Pseudopotential Fitting 1.109
7	N	$2p$	1	Pseudopotential Fitting 3.195
		$2s$	0	Pseudopotential Fitting 1.287
8	O	$2p$	1	Pseudopotential Fitting 3.564
		$2s$	0	Pseudopotential Fitting 1.403
9	F	$2p$	1	Pseudopotential Fitting 3.476
		$2s$	0	Pseudopotential Fitting 1.565
10	Ne	$2p$	1	Pseudopotential Fitting 4.326
		$2s$	0	Pseudopotential Fitting 1.516
11	Na	$3s$	0	Orthogonalization 1.516
		$2p$	1	Pseudopotential Fitting 3.456
		$3p$	1	Orthogonalization 3.456
		$3s$	0	Pseudopotential Fitting 0.414
12	Mg	$3p$	1	Pseudopotential Fitting 1.078
		$3s$	0	Pseudopotential Fitting 0.478
13	Al	$3p$	1	Pseudopotential Fitting 1.412
		$3s$	0	Pseudopotential Fitting 0.595
14	Si	$3p$	1	Pseudopotential Fitting 1.752
		$3s$	0	Pseudopotential Fitting 0.744
15	P	$3p$	1	Pseudopotential Fitting 2.117
		$3s$	0	Pseudopotential Fitting 0.722
16	S	$3p$	1	Pseudopotential Fitting 2.347
		$3s$	0	Pseudopotential Fitting 0.797
17	Cl	$3p$	1	Pseudopotential Fitting 2.637
		$3s$	0	Pseudopotential Fitting 1.057
18	Ar	$3p$	1	Pseudopotential Fitting 2.980
		$3s$	0	Pseudopotential Fitting 1.139
19	K	$4s$	0	Orthogonalization 1.139
		$3p$	1	Pseudopotential Fitting 3.410
		$4p$	1	Orthogonalization 3.410
		$3d$	2	OpenMX Fitting 2.727
		$3s$	0	Pseudopotential Fitting 1.266
20	Ca	$4s$	0	Orthogonalization 1.266
		$3p$	1	Pseudopotential Fitting 3.257
		$3d$	2	Pseudopotential Fitting 4.172
		$3s$	0	Pseudopotential Fitting 1.449
21	Sc	$4s$	0	Orthogonalization 1.449
		$3p$	1	Pseudopotential Fitting 4.074
		$3d$	2	Pseudopotential Fitting 5.810
		$4p$	1	Orthogonalization 4.074
22	Ti	$3s$	0	Pseudopotential Fitting 1.262
		$4s$	0	Orthogonalization 1.262
		$3p$	1	Pseudopotential Fitting 3.514
		$3d$	2	Pseudopotential Fitting 5.725
		$4p$	1	Orthogonalization 3.514

Z	Element	Orbital l	Source	$\alpha(\text{bohr}^{-1})$
23	V	3s	0	Pseudopotential Fitting 1.541
		4s	0	Orthogonalization 1.541
		3p	1	Pseudopotential Fitting 3.861
		3d	2	Pseudopotential Fitting 5.662
		4p	1	Orthogonalization 3.861
24	Cr	3s	0	Pseudopotential Fitting 1.598
		4s	0	Orthogonalization 1.598
		3p	1	Pseudopotential Fitting 3.949
		3d	2	Pseudopotential Fitting 5.999
		4p	1	Orthogonalization 3.949
25	Mn	3s	0	Pseudopotential Fitting 1.655
		4s	0	Orthogonalization 1.655
		3p	1	Pseudopotential Fitting 4.061
		4p	1	Orthogonalization 4.061
		3d	2	Pseudopotential Fitting 5.857
26	Fe	3s	0	Pseudopotential Fitting 1.804
		4s	0	Orthogonalization 1.804
		3p	1	Pseudopotential Fitting 4.925
		4p	1	Orthogonalization 4.925
		3d	2	Pseudopotential Fitting 5.248
27	Co	3s	0	Pseudopotential Fitting 1.656
		4s	0	Orthogonalization 1.656
		3p	1	Pseudopotential Fitting 3.888
		4p	1	Orthogonalization 3.888
		3d	2	Pseudopotential Fitting 6.165
28	Ni	3s	0	Pseudopotential Fitting 1.746
		4s	0	Orthogonalization 1.746
		3p	1	Pseudopotential Fitting 3.868
		4p	1	Orthogonalization 3.868
		3d	2	Pseudopotential Fitting 6.521
29	Cu	3s	0	Pseudopotential Fitting 1.674
		4s	0	Orthogonalization 1.674
		3p	1	Pseudopotential Fitting 3.477
		4p	1	Orthogonalization 3.477
		3d	2	Pseudopotential Fitting 6.327
30	Zn	3s	0	Pseudopotential Fitting 1.676
		4s	0	Orthogonalization 1.676
		3p	1	Pseudopotential Fitting 3.762
		4p	1	Orthogonalization 3.762
		3d	2	Pseudopotential Fitting 5.849
31	Ga	4s	0	Pseudopotential Fitting 0.558
		4p	1	Pseudopotential Fitting 1.484
		3d	2	Pseudopotential Fitting 5.166
32	Ge	4s	0	Pseudopotential Fitting 0.607
		4p	1	Pseudopotential Fitting 1.669
		3d	2	Pseudopotential Fitting 1.332
33	As	4s	0	Pseudopotential Fitting 0.710
		4p	1	Pseudopotential Fitting 1.984
34	Se	4s	0	Pseudopotential Fitting 0.668
		4p	1	Pseudopotential Fitting 2.068
35	Br	4s	0	Pseudopotential Fitting 0.713
		4p	1	Pseudopotential Fitting 2.267
36	Kr	4s	0	Pseudopotential Fitting 0.985
		4p	1	Pseudopotential Fitting 2.566
37	Rb	4s	0	Pseudopotential Fitting 1.099
		5s	0	Orthogonalization 1.099
		4p	1	Pseudopotential Fitting 2.894
		4d	2	OpenMX Fitting 2.197

Z	Element	Orbital l	Source	$\alpha(\text{bohr}^{-1})$
38	Sr	4s	0	Pseudopotential Fitting 1.064
		5s	0	Orthogonalization 1.064
		4p	1	Pseudopotential Fitting 3.045
		5p	1	Orthogonalization 3.045
		4d	2	Pseudopotential Fitting 3.121
39	Y	4s	0	Pseudopotential Fitting 1.164
		5s	0	Orthogonalization 1.164
		4p	1	Pseudopotential Fitting 3.058
		5p	1	Orthogonalization 3.058
		4d	2	Pseudopotential Fitting 3.940
40	Zr	4s	0	Pseudopotential Fitting 1.266
		5s	0	Orthogonalization 1.266
		4p	1	Pseudopotential Fitting 3.284
		5p	1	Orthogonalization 3.284
		4d	2	Pseudopotential Fitting 4.372
41	Nb	4s	0	Pseudopotential Fitting 1.356
		5s	0	Orthogonalization 1.356
		4p	1	Pseudopotential Fitting 3.700
		4d	2	Pseudopotential Fitting 5.157
		5p	1	Orthogonalization 3.700
42	Mo	4s	0	Pseudopotential Fitting 1.456
		5s	0	Orthogonalization 1.456
		4p	1	Pseudopotential Fitting 4.060
		4d	2	Pseudopotential Fitting 5.618
		5p	1	Orthogonalization 4.060
43	Tc	4s	0	Pseudopotential Fitting 1.556
		5s	0	Orthogonalization 1.556
		4p	1	Pseudopotential Fitting 4.215
		4d	2	Pseudopotential Fitting 5.984
		5p	1	Orthogonalization 4.215
44	Ru	4s	0	Pseudopotential Fitting 1.638
		5s	0	Orthogonalization 1.638
		4p	1	Pseudopotential Fitting 4.388
		4d	2	Pseudopotential Fitting 6.369
		5p	1	Orthogonalization 4.388
45	Rh	4s	0	Pseudopotential Fitting 1.700
		5s	0	Orthogonalization 1.700
		4p	1	Pseudopotential Fitting 4.505
		4d	2	Pseudopotential Fitting 6.670
		5p	1	Orthogonalization 4.505
46	Pd	4s	0	Pseudopotential Fitting 1.767
		5s	0	Orthogonalization 1.767
		4p	1	Pseudopotential Fitting 4.703
		4d	2	Pseudopotential Fitting 7.214
		5p	1	Orthogonalization 4.703
47	Ag	4s	0	Pseudopotential Fitting 1.820
		5s	0	Orthogonalization 1.820
		4p	1	Pseudopotential Fitting 4.835
		4d	2	Pseudopotential Fitting 7.455
		5p	1	Orthogonalization 4.835
48	Cd	5s	0	Pseudopotential Fitting 0.428
		5p	1	Pseudopotential Fitting 1.156
		4d	2	Pseudopotential Fitting 6.627
49	In	5s	0	Pseudopotential Fitting 0.433
		5p	1	Pseudopotential Fitting 1.320
		4d	2	Pseudopotential Fitting 6.051
50	Sn	5s	0	Pseudopotential Fitting 0.313
		5p	1	Pseudopotential Fitting 1.410
51	Sb	4d	2	Pseudopotential Fitting 5.547
		5s	0	Pseudopotential Fitting 0.347
		5p	1	Pseudopotential Fitting 1.557
		4d	2	Pseudopotential Fitting 6.769

Z	Element	Orbital l	Source	$\alpha(\text{bohr}^{-1})$
52	Te	$5s$	Pseudopotential Fitting	0.606
		$5p$	Pseudopotential Fitting	1.731
53	I	$5s$	Pseudopotential Fitting	0.684
		$5p$	Pseudopotential Fitting	1.840
54	Xe	$5s$	Pseudopotential Fitting	0.802
		$5p$	Pseudopotential Fitting	2.134
		$4d$	Pseudopotential Fitting	9.378
55	Cs	$5s$	Pseudopotential Fitting	0.826
		$6s$	Orthogonalization	0.826
		$5p$	Pseudopotential Fitting	2.284
		$6p$	Orthogonalization	2.284
		$5d$	Pseudopotential Fitting	1.993
56	Ba	$5s$	Pseudopotential Fitting	0.956
		$6s$	Orthogonalization	0.956
		$5p$	Pseudopotential Fitting	2.625
		$5d$	OpenMX Fitting	3.039
72	Hf	$5s$	Pseudopotential Fitting	1.338
		$6s$	Orthogonalization	1.338
		$5p$	Pseudopotential Fitting	3.698
		$5d$	Pseudopotential Fitting	4.275
		$6p$	Orthogonalization	3.698
73	Ta	$5s$	Pseudopotential Fitting	1.377
		$6s$	Orthogonalization	1.377
		$5p$	Pseudopotential Fitting	3.680
		$6p$	Orthogonalization	3.680
		$5d$	Pseudopotential Fitting	4.827
74	W	$5s$	Pseudopotential Fitting	1.443
		$6s$	Orthogonalization	1.443
		$5p$	Pseudopotential Fitting	3.786
		$6p$	Orthogonalization	3.786
		$5d$	Pseudopotential Fitting	5.147
75	Re	$5s$	Pseudopotential Fitting	1.473
		$6s$	Orthogonalization	1.473
		$5p$	Pseudopotential Fitting	3.874
		$6p$	Orthogonalization	3.874
		$5d$	Pseudopotential Fitting	5.504
76	Os	$5s$	Pseudopotential Fitting	1.534
		$6s$	Orthogonalization	1.534
		$5p$	Pseudopotential Fitting	4.074
		$6p$	Orthogonalization	4.074
		$5d$	Pseudopotential Fitting	5.950
77	Ir	$6s$	Pseudopotential Fitting	0.418
		$5p$	Pseudopotential Fitting	3.776
		$6p$	Orthogonalization	3.776
		$5d$	Pseudopotential Fitting	5.503
78	Pt	$6s$	Pseudopotential Fitting	0.436
		$5p$	Pseudopotential Fitting	3.993
		$6p$	Orthogonalization	3.993
		$5d$	Pseudopotential Fitting	5.852
79	Au	$5s$	Pseudopotential Fitting	1.840
		$6s$	Orthogonalization	1.840
		$5p$	Pseudopotential Fitting	4.682
		$5d$	Pseudopotential Fitting	6.697
		$6p$	Orthogonalization	4.682
80	Hg	$5s$	Pseudopotential Fitting	1.891
		$6s$	Orthogonalization	1.891
		$5p$	Pseudopotential Fitting	4.840
		$5d$	Pseudopotential Fitting	6.962
		$6p$	Orthogonalization	4.840
81	Tl	$6s$	Pseudopotential Fitting	0.548
		$6p$	Pseudopotential Fitting	1.219
		$5d$	Pseudopotential Fitting	4.322

Z	Element	Orbital l	Source	$\alpha(\text{bohr}^{-1})$
82	Pb	$6s$	Pseudopotential Fitting	0.607
		$6p$	Pseudopotential Fitting	1.477
		$5d$	Pseudopotential Fitting	5.953
83	Bi	$6s$	Pseudopotential Fitting	0.632
		$6p$	Pseudopotential Fitting	1.638
		$5d$	Pseudopotential Fitting	4.464
84	Po	$6s$	Pseudopotential Fitting	0.622
		$6p$	Pseudopotential Fitting	1.658
		$5d$	Pseudopotential Fitting	7.897
86	Rn	$6s$	Pseudopotential Fitting	0.615
		$6p$	Pseudopotential Fitting	1.915
		$5d$	Pseudopotential Fitting	8.335

SUPPLEMENTARY TABLE V: Values of α and minimal set of orbitals for the pseudopotentials of the PseudoDojo norm-conserving fully-relativistic v0.4 standard library with orthonormalization fitting.

Z	Element	Orbital l	j	Source	$\alpha(\text{bohr}^{-1})$
1	H	1s	0	0.5 Pseudopotential	—
2	He	1s	0	0.5 Pseudopotential	—
3	Li	1s	0	0.5 Pseudopotential	—
		2s	0	0.5 Pseudopotential	—
		2p	1	0.5 OpenMX Fitting	1.114
		2p	1	1.5 OpenMX Fitting	1.114
4	Be	1s	0	0.5 Pseudopotential	—
		2s	0	0.5 Pseudopotential	—
		2p	1	0.5 OpenMX Fitting	1.834
		2p	1	1.5 OpenMX Fitting	1.834
5	B	2s	0	0.5 Pseudopotential	—
		2p	1	0.5 Pseudopotential	—
		2p	1	1.5 Pseudopotential	—
		2s	0	0.5 Pseudopotential	—
6	C	2p	1	0.5 Pseudopotential	—
		2p	1	1.5 Pseudopotential	—
		2s	0	0.5 Pseudopotential	—
		2p	1	0.5 Pseudopotential	—
7	N	2p	1	0.5 Pseudopotential	—
		2p	1	1.5 Pseudopotential	—
		2s	0	0.5 Pseudopotential	—
		2p	1	0.5 Pseudopotential	—
8	O	2p	1	0.5 Pseudopotential	—
		2p	1	1.5 Pseudopotential	—
		2s	0	0.5 Pseudopotential	—
		2p	1	0.5 Pseudopotential	—
9	F	2p	1	0.5 Pseudopotential	—
		2p	1	1.5 Pseudopotential	—
		2s	0	0.5 Pseudopotential	—
		2p	1	0.5 Pseudopotential	—
10	Ne	2p	1	0.5 Pseudopotential	—
		2p	1	1.5 Pseudopotential	—
		2s	0	0.5 Pseudopotential	—
		2p	1	0.5 Pseudopotential	—
11	Na	2p	1	0.5 Pseudopotential	—
		2p	1	1.5 Pseudopotential	—
		3p	1	0.5 Orthogonalization	5.600
		3p	1	1.5 Orthogonalization	5.600
		2s	0	0.5 Pseudopotential	—
		3s	0	0.5 Pseudopotential	—
12	Mg	2p	1	0.5 Pseudopotential	—
		2p	1	1.5 Pseudopotential	—
		3p	1	0.5 Orthogonalization	6.500
		3p	1	1.5 Orthogonalization	6.400
		2s	0	0.5 Pseudopotential	—
		3s	0	0.5 Pseudopotential	—
13	Al	3p	1	0.5 Pseudopotential	—
		3p	1	1.5 Pseudopotential	—
		3s	0	0.5 Pseudopotential	—
14	Si	3p	1	0.5 Pseudopotential	—
		3p	1	1.5 Pseudopotential	—
		3s	0	0.5 Pseudopotential	—
15	P	3p	1	0.5 Pseudopotential	—
		3p	1	1.5 Pseudopotential	—
		3s	0	0.5 Pseudopotential	—
16	S	3p	1	0.5 Pseudopotential	—
		3p	1	1.5 Pseudopotential	—
		3s	0	0.5 Pseudopotential	—
17	Cl	3p	1	0.5 Pseudopotential	—
		3p	1	1.5 Pseudopotential	—
		3s	0	0.5 Pseudopotential	—
18	Ar	3p	1	0.5 Pseudopotential	—
		3p	1	1.5 Pseudopotential	—
		3s	0	0.5 Pseudopotential	—

Z	Element	Orbital l	j	Source	$\alpha(\text{bohr}^{-1})$
19	K	3s	0	0.5 Pseudopotential	—
		4s	0	0.5 Pseudopotential	—
		3p	1	0.5 Pseudopotential	—
		3p	1	1.5 Pseudopotential	—
		3d	2	1.5 OpenMX Fitting	2.727
		3d	2	2.5 OpenMX Fitting	2.727
20	Ca	3s	0	0.5 Pseudopotential	—
		4s	0	0.5 Pseudopotential	—
		3p	1	0.5 Pseudopotential	—
		3p	1	1.5 Pseudopotential	—
		3d	2	1.5 OpenMX Fitting	3.983
		3d	2	2.5 OpenMX Fitting	3.983
21	Sc	3s	0	0.5 Pseudopotential	—
		4s	0	0.5 Pseudopotential	—
		3p	1	0.5 Pseudopotential	—
		3p	1	1.5 Pseudopotential	—
		3d	2	1.5 Pseudopotential	—
		3d	2	2.5 Pseudopotential	—
22	Ti	4p	1	0.5 Orthogonalization	4.400
		4p	1	1.5 Orthogonalization	4.300
		3s	0	0.5 Pseudopotential	—
		4s	0	0.5 Pseudopotential	—
		3p	1	0.5 Pseudopotential	—
		3p	1	1.5 Pseudopotential	—
23	V	3d	2	1.5 Pseudopotential	—
		3d	2	2.5 Pseudopotential	—
		4p	1	0.5 Orthogonalization	5.000
		4p	1	1.5 Orthogonalization	5.000
		3s	0	0.5 Pseudopotential	—
		4s	0	0.5 Pseudopotential	—
24	Cr	3p	1	0.5 Pseudopotential	—
		3p	1	1.5 Pseudopotential	—
		3d	2	1.5 Pseudopotential	—
		3d	2	2.5 Pseudopotential	—
		4p	1	0.5 Orthogonalization	5.300
		4p	1	1.5 Orthogonalization	5.200
25	Mn	3s	0	0.5 Pseudopotential	—
		4s	0	0.5 Pseudopotential	—
		3p	1	0.5 Pseudopotential	—
		3p	1	1.5 Pseudopotential	—
		3d	2	1.5 Pseudopotential	—
		3d	2	2.5 Pseudopotential	—
26	Fe	4p	1	0.5 Orthogonalization	5.600
		4p	1	1.5 Orthogonalization	5.600
		3s	0	0.5 Pseudopotential	—
		4s	0	0.5 Pseudopotential	—
		3p	1	0.5 Pseudopotential	—
		3p	1	1.5 Pseudopotential	—
27	Co	3d	2	1.5 Pseudopotential	—
		3d	2	2.5 Pseudopotential	—
		4p	1	0.5 Orthogonalization	6.000
		4p	1	1.5 Orthogonalization	5.900
		3s	0	0.5 Pseudopotential	—
		4s	0	0.5 Pseudopotential	—

Z	Element	Orbital	l	j	Source	$\alpha(\text{bohr}^{-1})$
27	Co	3s	0	0.5	Pseudopotential	—
		4s	0	0.5	Pseudopotential	—
		3p	1	0.5	Pseudopotential	—
		3p	1	1.5	Pseudopotential	—
		3d	2	1.5	Pseudopotential	—
		3d	2	2.5	Pseudopotential	—
		4p	1	0.5	Orthogonalization	6.300
		4p	1	1.5	Orthogonalization	6.200
28	Ni	3s	0	0.5	Pseudopotential	—
		4s	0	0.5	Pseudopotential	—
		3p	1	0.5	Pseudopotential	—
		3p	1	1.5	Pseudopotential	—
		3d	2	1.5	Pseudopotential	—
		3d	2	2.5	Pseudopotential	—
		4p	1	0.5	Orthogonalization	6.500
		4p	1	1.5	Orthogonalization	6.500
29	Cu	3s	0	0.5	Pseudopotential	—
		4s	0	0.5	Pseudopotential	—
		3p	1	0.5	Pseudopotential	—
		3p	1	1.5	Pseudopotential	—
		3d	2	1.5	Pseudopotential	—
		3d	2	2.5	Pseudopotential	—
		4p	1	0.5	Orthogonalization	6.700
		4p	1	1.5	Orthogonalization	6.600
30	Zn	3s	0	0.5	Pseudopotential	—
		4s	0	0.5	Pseudopotential	—
		3p	1	0.5	Pseudopotential	—
		3p	1	1.5	Pseudopotential	—
		3d	2	1.5	Pseudopotential	—
		3d	2	2.5	Pseudopotential	—
		4p	1	0.5	Orthogonalization	6.900
		4p	1	1.5	Orthogonalization	6.800
31	Ga	4s	0	0.5	Pseudopotential	—
		4p	1	0.5	Pseudopotential	—
		4p	1	1.5	Pseudopotential	—
		3d	2	1.5	Pseudopotential	—
		3d	2	2.5	Pseudopotential	—
32	Ge	4s	0	0.5	Pseudopotential	—
		4p	1	0.5	Pseudopotential	—
		4p	1	1.5	Pseudopotential	—
		3d	2	1.5	Pseudopotential	—
		3d	2	2.5	Pseudopotential	—
33	As	4s	0	0.5	Pseudopotential	—
		4p	1	0.5	Pseudopotential	—
		4p	1	1.5	Pseudopotential	—
		3d	2	1.5	Pseudopotential	—
		3d	2	2.5	Pseudopotential	—
34	Se	4s	0	0.5	Pseudopotential	—
		4p	1	0.5	Pseudopotential	—
		4p	1	1.5	Pseudopotential	—
		3d	2	1.5	Pseudopotential	—
		3d	2	2.5	Pseudopotential	—
35	Br	4s	0	0.5	Pseudopotential	—
		4p	1	0.5	Pseudopotential	—
		4p	1	1.5	Pseudopotential	—
36	Kr	4s	0	0.5	Pseudopotential	—
		4p	1	0.5	Pseudopotential	—
		4p	1	1.5	Pseudopotential	—

Z	Element	Orbital	l	j	Source	$\alpha(\text{bohr}^{-1})$
37	Rb	4s	0	0.5	Pseudopotential	—
		5s	0	0.5	Pseudopotential	—
		4p	1	0.5	Pseudopotential	—
		4p	1	1.5	Pseudopotential	—
		4d	2	1.5	OpenMX Fitting	2.197
		4d	2	2.5	OpenMX Fitting	2.197
		4d	2	2.5	OpenMX Fitting	2.197
38	Sr	4s	0	0.5	Pseudopotential	—
		5s	0	0.5	Pseudopotential	—
		4p	1	0.5	Pseudopotential	—
		4p	1	1.5	Pseudopotential	—
		4d	2	1.5	OpenMX Fitting	4.400
39	Y	4d	2	2.5	OpenMX Fitting	4.400
		4s	0	0.5	Pseudopotential	—
		5s	0	0.5	Pseudopotential	—
		4p	1	0.5	Pseudopotential	—
		4p	1	1.5	Pseudopotential	—
40	Zr	4d	2	1.5	Pseudopotential	—
		4d	2	2.5	Pseudopotential	—
		5p	1	0.5	Orthogonalization	3.600
		5p	1	1.5	Orthogonalization	3.500
		4s	0	0.5	Pseudopotential	—
41	Nb	5s	0	0.5	Pseudopotential	—
		4p	1	0.5	Pseudopotential	—
		4p	1	1.5	Pseudopotential	—
		4d	2	1.5	Pseudopotential	—
		4d	2	2.5	Pseudopotential	—
42	Mo	5p	1	0.5	Orthogonalization	4.000
		5p	1	1.5	Orthogonalization	3.900
		4s	0	0.5	Pseudopotential	—
		5s	0	0.5	Pseudopotential	—
		4p	1	0.5	Pseudopotential	—
43	Tc	4p	1	1.5	Pseudopotential	—
		4d	2	1.5	Pseudopotential	—
		4d	2	2.5	Pseudopotential	—
		5p	1	0.5	Orthogonalization	4.300
		5p	1	1.5	Orthogonalization	4.200
44	Ru	4s	0	0.5	Pseudopotential	—
		5s	0	0.5	Pseudopotential	—
		4p	1	0.5	Pseudopotential	—
		4p	1	1.5	Pseudopotential	—
		4d	2	1.5	Pseudopotential	—
45	Rh	4d	2	2.5	Pseudopotential	—
		5p	1	0.5	Orthogonalization	4.700
		5p	1	1.5	Orthogonalization	4.600
		4s	0	0.5	Pseudopotential	—
		5s	0	0.5	Pseudopotential	—

Z	Element	Orbital	l	j	Source	$\alpha(\text{bohr}^{-1})$
45	Rh	4s	0	0.5	Pseudopotential	—
		5s	0	0.5	Pseudopotential	—
		4p	1	0.5	Pseudopotential	—
		4p	1	1.5	Pseudopotential	—
		4d	2	1.5	Pseudopotential	—
		4d	2	2.5	Pseudopotential	—
		5p	1	0.5	Orthogonalization	4.900
		5p	1	1.5	Orthogonalization	4.800
46	Pd	4s	0	0.5	Pseudopotential	—
		4p	1	0.5	Pseudopotential	—
		4p	1	1.5	Pseudopotential	—
		4d	2	1.5	Pseudopotential	—
		4d	2	2.5	Pseudopotential	—
		5s	0	0.5	Orthogonalization	1.900
		5p	1	0.5	Orthogonalization	5.100
		5p	1	1.5	Orthogonalization	4.900
47	Ag	4s	0	0.5	Pseudopotential	—
		5s	0	0.5	Pseudopotential	—
		4p	1	0.5	Pseudopotential	—
		4p	1	1.5	Pseudopotential	—
		4d	2	1.5	Pseudopotential	—
		4d	2	2.5	Pseudopotential	—
		5p	1	0.5	Orthogonalization	5.400
		5p	1	1.5	Orthogonalization	5.200
48	Cd	4s	0	0.5	Pseudopotential	—
		5s	0	0.5	Pseudopotential	—
		4p	1	0.5	Pseudopotential	—
		4p	1	1.5	Pseudopotential	—
		4d	2	1.5	Pseudopotential	—
		4d	2	2.5	Pseudopotential	—
		5p	1	0.5	Orthogonalization	5.600
		5p	1	1.5	Orthogonalization	5.400
49	In	5s	0	0.5	Pseudopotential	—
		5p	1	0.5	Pseudopotential	—
		5p	1	1.5	Pseudopotential	—
		4d	2	1.5	Pseudopotential	—
50	Sn	4d	2	2.5	Pseudopotential	—
		5s	0	0.5	Pseudopotential	—
		5p	1	0.5	Pseudopotential	—
		5p	1	1.5	Pseudopotential	—
51	Sb	4d	2	1.5	Pseudopotential	—
		4d	2	2.5	Pseudopotential	—
		5s	0	0.5	Pseudopotential	—
		5p	1	0.5	Pseudopotential	—
52	Te	5p	1	1.5	Pseudopotential	—
		4d	2	1.5	Pseudopotential	—
		4d	2	2.5	Pseudopotential	—
		5s	0	0.5	Pseudopotential	—
53	I	5p	1	0.5	Pseudopotential	—
		5p	1	1.5	Pseudopotential	—
		5s	0	0.5	Pseudopotential	—
54	Xe	5p	1	0.5	Pseudopotential	—
		5p	1	1.5	Pseudopotential	—
		5s	0	0.5	Pseudopotential	—

Z	Element	Orbital	l	j	Source	$\alpha(\text{bohr}^{-1})$
55	Cs	5s	0	0.5	Pseudopotential	—
		6s	0	0.5	Pseudopotential	—
		5p	1	0.5	Pseudopotential	—
		5p	1	1.5	Pseudopotential	—
		5d	2	1.5	OpenMX Fitting	3.566
		5d	2	2.5	OpenMX Fitting	3.566
56	Ba	5s	0	0.5	Pseudopotential	—
		6s	0	0.5	Pseudopotential	—
		5p	1	0.5	Pseudopotential	—
		5p	1	1.5	Pseudopotential	—
		5d	2	1.5	OpenMX Fitting	3.039
72	Hf	5d	2	2.5	OpenMX Fitting	3.039
		5s	0	0.5	Pseudopotential	—
		6s	0	0.5	Pseudopotential	—
		5p	1	0.5	Pseudopotential	—
		5p	1	1.5	Pseudopotential	—
		5d	2	1.5	Pseudopotential	—
73	Ta	5d	2	2.5	Pseudopotential	—
		6p	1	0.5	Orthogonalization	4.200
		6p	1	1.5	Orthogonalization	3.800
		5s	0	0.5	Pseudopotential	—
		6s	0	0.5	Pseudopotential	—
74	W	5p	1	0.5	Pseudopotential	—
		5p	1	1.5	Pseudopotential	—
		5d	2	1.5	Pseudopotential	—
		5d	2	2.5	Pseudopotential	—
		6p	1	0.5	Orthogonalization	4.500
		6p	1	1.5	Orthogonalization	4.100
75	Re	5s	0	0.5	Pseudopotential	—
		6s	0	0.5	Pseudopotential	—
		5p	1	0.5	Pseudopotential	—
		5p	1	1.5	Pseudopotential	—
		5d	2	1.5	Pseudopotential	—
		5d	2	2.5	Pseudopotential	—
76	Os	6p	1	0.5	Orthogonalization	4.700
		6p	1	1.5	Orthogonalization	4.300
		5s	0	0.5	Pseudopotential	—
		6s	0	0.5	Pseudopotential	—
		5p	1	0.5	Pseudopotential	—
		5p	1	1.5	Pseudopotential	—
77	Ir	5d	2	1.5	Pseudopotential	—
		5d	2	2.5	Pseudopotential	—
		6p	1	0.5	Orthogonalization	5.000
		6p	1	1.5	Orthogonalization	4.600
		5s	0	0.5	Pseudopotential	—
		6s	0	0.5	Pseudopotential	—

Z	Element	Orbital l	j	Source	$\alpha(\text{bohr}^{-1})$
78	Pt	5s	0	0.5 Pseudopotential	—
		6s	0	0.5 Pseudopotential	—
		5p	1	0.5 Pseudopotential	—
		5p	1	1.5 Pseudopotential	—
		5d	2	1.5 Pseudopotential	—
		5d	2	2.5 Pseudopotential	—
		6p	1	0.5 Orthogonalization	5.100
		6p	1	1.5 Orthogonalization	4.600
79	Au	5s	0	0.5 Pseudopotential	—
		6s	0	0.5 Pseudopotential	—
		5p	1	0.5 Pseudopotential	—
		5p	1	1.5 Pseudopotential	—
		5d	2	1.5 Pseudopotential	—
		5d	2	2.5 Pseudopotential	—
		6p	1	0.5 Orthogonalization	5.300
		6p	1	1.5 Orthogonalization	4.800
80	Hg	5s	0	0.5 Pseudopotential	—
		6s	0	0.5 Pseudopotential	—
		5p	1	0.5 Pseudopotential	—
		5p	1	1.5 Pseudopotential	—
		5d	2	1.5 Pseudopotential	—
		5d	2	2.5 Pseudopotential	—
		6p	1	0.5 Orthogonalization	5.500
		6p	1	1.5 Orthogonalization	5.000
81	Tl	6s	0	0.5 Pseudopotential	—
		6p	1	0.5 Pseudopotential	—
		6p	1	1.5 Pseudopotential	—
		5d	2	1.5 Pseudopotential	—
		5d	2	2.5 Pseudopotential	—
82	Pb	6s	0	0.5 Pseudopotential	—
		6p	1	0.5 Pseudopotential	—
		6p	1	1.5 Pseudopotential	—
		5d	2	1.5 Pseudopotential	—
		5d	2	2.5 Pseudopotential	—
83	Bi	6s	0	0.5 Pseudopotential	—
		6p	1	0.5 Pseudopotential	—
		6p	1	1.5 Pseudopotential	—
		5d	2	1.5 Pseudopotential	—
		5d	2	2.5 Pseudopotential	—
84	Po	6s	0	0.5 Pseudopotential	—
		6p	1	0.5 Pseudopotential	—
		6p	1	1.5 Pseudopotential	—
		5d	2	1.5 Pseudopotential	—
		5d	2	2.5 Pseudopotential	—
86	Rn	6s	0	0.5 Pseudopotential	—
		6p	1	0.5 Pseudopotential	—
		6p	1	1.5 Pseudopotential	—
		5d	2	1.5 Pseudopotential	—
		5d	2	2.5 Pseudopotential	—

SUPPLEMENTARY TABLE VI: Source of the pseudopotentials in the **modified-pslibrary** set. We started by selecting pseudopotentials based on the suggested list [4] from pslibrary. However, during DFT calculations, we encountered convergence errors with certain pseudopotentials. Thus, some pseudopotentials were replaced with either older versions from pslibrary or alternatives from pseudoDojo, as reported in this table.

Z	Elem.	Source	Filename
1	H	pslibrary	H.rel-pbe-kjpaw_psl.1.0.0.UPF
2	He	pslibrary	He.rel-pbe-kjpaw_psl.1.0.0.UPF
3	Li	pslibrary	Li.rel-pbe-sl-kjpaw_psl.1.0.0.UPF
4	Be	pslibrary	Be.rel-pbe-sl-kjpaw_psl.1.0.0.UPF
5	B	pslibrary	B.rel-pbe-n-kjpaw_psl.1.0.0.UPF
6	C	pslibrary	C.rel-pbe-n-kjpaw_psl.1.0.0.UPF
7	N	pslibrary	N.rel-pbe-n-kjpaw_psl.1.0.0.UPF
8	O	pslibrary	O.rel-pbe-n-kjpaw_psl.0.1.UPF
9	F	pslibrary	F.rel-pbe-n-kjpaw_psl.1.0.0.UPF
10	Ne	pslibrary	Ne.rel-pbe-n-kjpaw_psl.1.0.0.UPF
11	Na	pslibrary	Na.rel-pbe-spn-kjpaw_psl.1.0.0.UPF
12	Mg	pslibrary	Mg.rel-pbe-spn-kjpaw_psl.1.0.0.UPF
13	Al	pslibrary	Al.rel-pbe-nl-kjpaw_psl.1.0.0.UPF
14	Si	pslibrary	Si.rel-pbe-nl-kjpaw_psl.1.0.0.UPF
15	P	pslibrary	P.rel-pbe-nl-kjpaw_psl.1.0.0.UPF
16	S	pslibrary	S.rel-pbe-nl-kjpaw_psl.1.0.0.UPF
17	Cl	pslibrary	Cl.rel-pbe-nl-kjpaw_psl.1.0.0.UPF
18	Ar	pslibrary	Ar.rel-pbe-nl-kjpaw_psl.1.0.0.UPF
19	K	pslibrary	K.rel-pbe-spn-kjpaw_psl.1.0.0.UPF
20	Ca	pslibrary	Ca.rel-pbe-spn-kjpaw_psl.1.0.0.UPF
21	Sc	pslibrary	Sc.rel-pbe-spn-kjpaw_psl.1.0.0.UPF
22	Ti	pslibrary	Ti.rel-pbe-spn-kjpaw_psl.1.0.0.UPF
23	V	pslibrary	V.rel-pbe-spn-kjpaw_psl.1.0.0.UPF
24	Cr	pslibrary	Cr.rel-pbe-spn-kjpaw_psl.1.0.0.UPF
25	Mn	pslibrary	Mn.rel-pbe-spn-kjpaw_psl.0.3.1.UPF
26	Fe	pslibrary	Fe.rel-pbe-n-kjpaw_psl.0.2.4.UPF
27	Co	pslibrary	Co.rel-pbe-spn-kjpaw_psl.0.3.1.UPF
28	Ni	pslibrary	Ni.rel-pbe-n-kjpaw_psl.0.1.UPF
29	Cu	pslibrary	Cu.rel-pbe-dn-kjpaw_psl.1.0.0.UPF
30	Zn	pslibrary	Zn.rel-pbe-dn-kjpaw_psl.1.0.0.UPF
31	Ga	pslibrary	Ga.rel-pbe-dnl-kjpaw_psl.1.0.0.UPF
32	Ge	pslibrary	Ge.rel-pbe-n-kjpaw_psl.1.0.0.UPF
33	As	pslibrary	As.rel-pbe-n-kjpaw_psl.1.0.0.UPF
34	Se	pslibrary	Se.rel-pbe-n-kjpaw_psl.1.0.0.UPF
35	Br	pslibrary	Br.rel-pbe-n-kjpaw_psl.1.0.0.UPF
36	Kr	pslibrary	Kr.rel-pbe-dn-kjpaw_psl.1.0.0.UPF
37	Rb	pslibrary	Rb.rel-pbe-spn-kjpaw_psl.1.0.0.UPF
38	Sr	pslibrary	Sr.rel-pbe-spn-kjpaw_psl.1.0.0.UPF
39	Y	pslibrary	Y.rel-pbe-spn-kjpaw_psl.1.0.0.UPF
40	Zr	pslibrary	Zr.rel-pbe-spn-kjpaw_psl.1.0.0.UPF
41	Nb	pslibrary	Nb.rel-pbe-spn-kjpaw_psl.1.0.0.UPF
42	Mo	pslibrary	Mo.rel-pbe-spn-kjpaw_psl.1.0.0.UPF
43	Tc	pslibrary	Tc.rel-pbe-spn-kjpaw_psl.0.3.0.UPF
44	Ru	pslibrary	Ru.rel-pbe-spn-kjpaw_psl.1.0.0.UPF
45	Rh	pseudoDojo	Rh.UPF
46	Pd	pslibrary	Pd.rel-pbe-n-kjpaw_psl.1.0.0.UPF
47	Ag	pslibrary	Ag.rel-pbe-n-kjpaw_psl.1.0.0.UPF
48	Cd	pslibrary	Cd.rel-pbe-dn-kjpaw_psl.0.3.1.UPF
49	In	pslibrary	In.rel-pbe-dn-kjpaw_psl.1.0.0.UPF
50	Sn	pslibrary	Sn.rel-pbe-dn-kjpaw_psl.1.0.0.UPF
51	Sb	pslibrary	Sb.rel-pbe-n-kjpaw_psl.1.0.0.UPF
52	Te	pslibrary	Te.rel-pbe-n-kjpaw_psl.1.0.0.UPF
53	I	pslibrary	I.rel-pbe-n-kjpaw_psl.1.0.0.UPF
54	Xe	pslibrary	Xe.rel-pbe-dn-kjpaw_psl.1.0.0.UPF
55	Cs	pseudoDojo	Cs.UPF

Z	Elem.	Source	Filename
56	Ba	pslibrary	Ba.rel-pbe-spn-kjpaw_psl.1.0.0.UPF
72	Hf	pslibrary	Hf.rel-pbe-spn-kjpaw_psl.1.0.0.UPF
73	Ta	pslibrary	Ta.rel-pbe-spn-kjpaw_psl.0.2.UPF
74	W	pslibrary	W.rel-pbe-spn-kjpaw_psl.1.0.1.UPF
75	Re	pslibrary	Re.rel-pbe-spn-kjpaw_psl.1.0.0.UPF
76	Os	pslibrary	Os.rel-pbe-spn-kjpaw_psl.1.0.0.UPF
77	Ir	pslibrary	Ir.rel-pbe-n-kjpaw_psl.0.2.3.UPF
78	Pt	pslibrary	Pt.rel-pbe-n-kjpaw_psl.1.0.0.UPF
79	Au	pslibrary	Au.rel-pbe-n-kjpaw_psl.1.0.0.UPF
80	Hg	pslibrary	Hg.rel-pbe-n-kjpaw_psl.1.0.0.UPF
81	Tl	pslibrary	Tl.rel-pbe-dn-kjpaw_psl.1.0.0.UPF
82	Pb	pslibrary	Pb.rel-pbe-dn-kjpaw_psl.0.2.2.UPF
83	Bi	pslibrary	Bi.rel-pbe-dn-kjpaw_psl.1.0.0.UPF
84	Po	pslibrary	Po.rel-pbe-dn-kjpaw_psl.1.0.0.UPF
85	At	pslibrary	At.rel-pbe-dn-kjpaw_psl.1.0.0.UPF
86	Rn	pslibrary	Rn.rel-pbe-dn-kjpaw_psl.1.0.0.UPF
87	Fr	pslibrary	Fr.rel-pbe-spdn-kjpaw_psl.1.0.0.UPF
88	Ra	pslibrary	Ra.rel-pbe-spdn-kjpaw_psl.1.0.0.UPF

SUPPLEMENTARY TABLE VII: Values of α and minimal set of orbitals for the pseudopotentials of the **modified-pslibrary** set with orthonormalization fitting.

Z	Element	Orbital	l	j	Source	$\alpha(\text{bohr}^{-1})$
1	H	1s	0	0.5	Pseudopotential	—
2	He	1s	0	0.5	Pseudopotential	—
3	Li	1s	0	0.5	Pseudopotential	—
		2s	0	0.5	Pseudopotential	—
		2p	1	0.5	Pseudopotential	—
		2p	1	1.5	Pseudopotential	—
4	Be	1s	0	0.5	Pseudopotential	—
		2s	0	0.5	Pseudopotential	—
		2p	1	0.5	Pseudopotential	—
		2p	1	1.5	Pseudopotential	—
5	B	2s	0	0.5	Pseudopotential	—
		2p	1	0.5	Pseudopotential	—
		2p	1	1.5	Pseudopotential	—
		2s	0	0.5	Pseudopotential	—
6	C	2p	1	0.5	Pseudopotential	—
		2p	1	1.5	Pseudopotential	—
		2s	0	0.5	Pseudopotential	—
		2p	1	0.5	Pseudopotential	—
7	N	2p	1	0.5	Pseudopotential	—
		2p	1	1.5	Pseudopotential	—
		2s	0	0.5	Pseudopotential	—
		2p	1	0.5	Pseudopotential	—
8	O	2p	1	0.5	Pseudopotential	—
		2p	1	1.5	Pseudopotential	—
		2s	0	0.5	Pseudopotential	—
		2p	1	0.5	Pseudopotential	—
9	F	2p	1	0.5	Pseudopotential	—
		2p	1	1.5	Pseudopotential	—
		2s	0	0.5	Pseudopotential	—
		2p	1	0.5	Pseudopotential	—
10	Ne	2p	1	0.5	Pseudopotential	—
		2p	1	1.5	Pseudopotential	—
		2s	0	0.5	Pseudopotential	—
		3s	0	0.5	Pseudopotential	—
11	Na	2p	1	0.5	Pseudopotential	—
		2p	1	1.5	Pseudopotential	—
		3p	1	0.5	Orthogonalization	4.900
		3p	1	1.5	Orthogonalization	4.900
		2s	0	0.5	Pseudopotential	—
		3s	0	0.5	Pseudopotential	—
12	Mg	2p	1	0.5	Pseudopotential	—
		2p	1	1.5	Pseudopotential	—
		3p	1	0.5	Orthogonalization	5.500
		3p	1	1.5	Orthogonalization	5.500
		3s	0	0.5	Pseudopotential	—
		3p	1	0.5	Pseudopotential	—
13	Al	3p	1	1.5	Pseudopotential	—
		3p	1	0.5	Pseudopotential	—
		3s	0	0.5	Pseudopotential	—
14	Si	3p	1	0.5	Pseudopotential	—
		3p	1	1.5	Pseudopotential	—
		3s	0	0.5	Pseudopotential	—
15	P	3p	1	0.5	Pseudopotential	—
		3p	1	1.5	Pseudopotential	—
		3s	0	0.5	Pseudopotential	—
16	S	3p	1	0.5	Pseudopotential	—
		3p	1	1.5	Pseudopotential	—
		3s	0	0.5	Pseudopotential	—
17	Cl	3p	1	0.5	Pseudopotential	—
		3p	1	1.5	Pseudopotential	—
		3s	0	0.5	Pseudopotential	—
18	Ar	3p	1	0.5	Pseudopotential	—
		3p	1	1.5	Pseudopotential	—
		3s	0	0.5	Pseudopotential	—

Z	Element	Orbital	l	j	Source	$\alpha(\text{bohr}^{-1})$
19	K	3s	0	0.5	Pseudopotential	—
		4s	0	0.5	Pseudopotential	—
		3p	1	0.5	Pseudopotential	—
		4p	1	0.5	Pseudopotential	—
		3p	1	1.5	Pseudopotential	—
		4p	1	1.5	Pseudopotential	—
		3d	2	1.5	OpenMX Fitting	2.727
		3d	2	2.5	OpenMX Fitting	2.727
20	Ca	3s	0	0.5	Pseudopotential	—
		4s	0	0.5	Pseudopotential	—
		3p	1	0.5	Pseudopotential	—
		4p	1	0.5	Pseudopotential	—
		3p	1	1.5	Pseudopotential	—
		4p	1	1.5	Pseudopotential	—
		3d	2	1.5	OpenMX Fitting	3.983
		3d	2	2.5	OpenMX Fitting	3.983
21	Sc	3s	0	0.5	Pseudopotential	—
		4s	0	0.5	Pseudopotential	—
		3p	1	0.5	Pseudopotential	—
		3p	1	1.5	Pseudopotential	—
		3d	2	1.5	Pseudopotential	—
		3d	2	2.5	Pseudopotential	—
		4p	1	0.5	Orthogonalization	4.400
		4p	1	1.5	Orthogonalization	4.400
22	Ti	3s	0	0.5	Pseudopotential	—
		4s	0	0.5	Pseudopotential	—
		3p	1	0.5	Pseudopotential	—
		3p	1	1.5	Pseudopotential	—
		3d	2	1.5	Pseudopotential	—
		3d	2	2.5	Pseudopotential	—
		4p	1	0.5	Orthogonalization	4.600
		4p	1	1.5	Orthogonalization	4.500
23	V	3s	0	0.5	Pseudopotential	—
		4s	0	0.5	Pseudopotential	—
		3p	1	0.5	Pseudopotential	—
		3p	1	1.5	Pseudopotential	—
		3d	2	1.5	Pseudopotential	—
		3d	2	2.5	Pseudopotential	—
		4p	1	0.5	Orthogonalization	5.000
		4p	1	1.5	Orthogonalization	4.900
24	Cr	3s	0	0.5	Pseudopotential	—
		4s	0	0.5	Pseudopotential	—
		3p	1	0.5	Pseudopotential	—
		3p	1	1.5	Pseudopotential	—
		3d	2	1.5	Pseudopotential	—
		3d	2	2.5	Pseudopotential	—
		4p	1	0.5	Orthogonalization	5.200
		4p	1	1.5	Orthogonalization	5.200
25	Mn	3s	0	0.5	Pseudopotential	—
		4s	0	0.5	Pseudopotential	—
		3p	1	0.5	Pseudopotential	—
		3p	1	1.5	Pseudopotential	—
		3d	2	1.5	Pseudopotential	—
		3d	2	2.5	Pseudopotential	—
		4p	1	0.5	Orthogonalization	4.700
		4p	1	1.5	Orthogonalization	4.700
26	Fe	4s	0	0.5	Pseudopotential	—
		4p	1	0.5	Pseudopotential	—
		4p	1	1.5	Pseudopotential	—
		3d	2	1.5	Pseudopotential	—
		3d	2	2.5	Pseudopotential	—

Z	Element	Orbital	l	j	Source	$\alpha(\text{bohr}^{-1})$
27	Co	3s	0	0.5	Pseudopotential	—
		4s	0	0.5	Pseudopotential	—
		3p	1	0.5	Pseudopotential	—
		3p	1	1.5	Pseudopotential	—
		3d	2	1.5	Pseudopotential	—
		3d	2	2.5	Pseudopotential	—
		4p	1	0.5	Orthogonalization	5.900
		4p	1	1.5	Orthogonalization	5.900
28	Ni	4s	0	0.5	Pseudopotential	—
		4p	1	0.5	Pseudopotential	—
		4p	1	1.5	Pseudopotential	—
		3d	2	1.5	Pseudopotential	—
		3d	2	2.5	Pseudopotential	—
29	Cu	4s	0	0.5	Pseudopotential	—
		4p	1	0.5	Pseudopotential	—
		4p	1	1.5	Pseudopotential	—
		3d	2	1.5	Pseudopotential	—
		3d	2	2.5	Pseudopotential	—
30	Zn	4s	0	0.5	Pseudopotential	—
		4p	1	0.5	Pseudopotential	—
		4p	1	1.5	Pseudopotential	—
		3d	2	1.5	Pseudopotential	—
		3d	2	2.5	Pseudopotential	—
31	Ga	4s	0	0.5	Pseudopotential	—
		4p	1	0.5	Pseudopotential	—
		4p	1	1.5	Pseudopotential	—
		3d	2	1.5	Pseudopotential	—
		3d	2	2.5	Pseudopotential	—
32	Ge	4s	0	0.5	Pseudopotential	—
		4p	1	0.5	Pseudopotential	—
		4p	1	1.5	Pseudopotential	—
33	As	4s	0	0.5	Pseudopotential	—
		4p	1	0.5	Pseudopotential	—
		4p	1	1.5	Pseudopotential	—
34	Se	4s	0	0.5	Pseudopotential	—
		4p	1	0.5	Pseudopotential	—
		4p	1	1.5	Pseudopotential	—
35	Br	4s	0	0.5	Pseudopotential	—
		4p	1	0.5	Pseudopotential	—
		4p	1	1.5	Pseudopotential	—
36	Kr	4s	0	0.5	Pseudopotential	—
		4p	1	0.5	Pseudopotential	—
		4p	1	1.5	Pseudopotential	—
		3d	2	1.5	Pseudopotential	—
		3d	2	2.5	Pseudopotential	—
37	Rb	4s	0	0.5	Pseudopotential	—
		5s	0	0.5	Pseudopotential	—
		4p	1	0.5	Pseudopotential	—
		5p	1	0.5	Pseudopotential	—
		4p	1	1.5	Pseudopotential	—
		5p	1	1.5	Pseudopotential	—
		4d	2	1.5	OpenMX Fitting	2.197
38	Sr	4d	2	2.5	OpenMX Fitting	2.197
		4s	0	0.5	Pseudopotential	—
		5s	0	0.5	Pseudopotential	—
		4p	1	0.5	Pseudopotential	—
		5p	1	0.5	Pseudopotential	—
		4p	1	1.5	Pseudopotential	—
		5p	1	1.5	Pseudopotential	—
		4d	2	1.5	OpenMX Fitting	4.400
		4d	2	2.5	OpenMX Fitting	4.400

Z	Element	Orbital	l	j	Source	$\alpha(\text{bohr}^{-1})$
39	Y	4s	0	0.5	Pseudopotential	—
		5s	0	0.5	Pseudopotential	—
		4p	1	0.5	Pseudopotential	—
		5p	1	0.5	Pseudopotential	—
		4p	1	1.5	Pseudopotential	—
		5p	1	1.5	Pseudopotential	—
		4d	2	1.5	Pseudopotential	—
		4d	2	2.5	Pseudopotential	—
40	Zr	4s	0	0.5	Pseudopotential	—
		5s	0	0.5	Pseudopotential	—
		4p	1	0.5	Pseudopotential	—
		5p	1	0.5	Pseudopotential	—
		4p	1	1.5	Pseudopotential	—
		5p	1	1.5	Pseudopotential	—
		4d	2	1.5	Pseudopotential	—
		4d	2	2.5	Pseudopotential	—
41	Nb	4s	0	0.5	Pseudopotential	—
		5s	0	0.5	Pseudopotential	—
		4p	1	0.5	Pseudopotential	—
		5p	1	0.5	Pseudopotential	—
		4p	1	1.5	Pseudopotential	—
		5p	1	1.5	Pseudopotential	—
		4d	2	1.5	Pseudopotential	—
		4d	2	2.5	Pseudopotential	—
42	Mo	4s	0	0.5	Pseudopotential	—
		5s	0	0.5	Pseudopotential	—
		4p	1	0.5	Pseudopotential	—
		4p	1	1.5	Pseudopotential	—
		4d	2	1.5	Pseudopotential	—
		4d	2	2.5	Pseudopotential	—
		5p	1	0.5	Orthogonalization	4.500
		5p	1	1.5	Orthogonalization	4.400
43	Tc	4s	0	0.5	Pseudopotential	—
		5s	0	0.5	Pseudopotential	—
		4p	1	0.5	Pseudopotential	—
		5p	1	0.5	Pseudopotential	—
		4p	1	1.5	Pseudopotential	—
		5p	1	1.5	Pseudopotential	—
		4d	2	1.5	Pseudopotential	—
		4d	2	2.5	Pseudopotential	—
44	Ru	4s	0	0.5	Pseudopotential	—
		5s	0	0.5	Pseudopotential	—
		4p	1	0.5	Pseudopotential	—
		4p	1	1.5	Pseudopotential	—
		4d	2	1.5	Pseudopotential	—
		4d	2	2.5	Pseudopotential	—
		5p	1	0.5	Orthogonalization	4.900
		5p	1	1.5	Orthogonalization	4.800
45	Rh	4s	0	0.5	Pseudopotential	—
		5s	0	0.5	Pseudopotential	—
		4p	1	0.5	Pseudopotential	—
		4p	1	1.5	Pseudopotential	—
		4d	2	1.5	Pseudopotential	—
		4d	2	2.5	Pseudopotential	—
		5p	1	0.5	Orthogonalization	4.900
		5p	1	1.5	Orthogonalization	4.800
46	Pd	5s	0	0.5	Pseudopotential	—
		5p	1	0.5	Pseudopotential	—
		5p	1	1.5	Pseudopotential	—
		4d	2	1.5	Pseudopotential	—
		4d	2	2.5	Pseudopotential	—

Z	Element	Orbital	l	j	Source	$\alpha(\text{bohr}^{-1})$
47	Ag	5s	0	0.5	Pseudopotential	—
		5p	1	0.5	Pseudopotential	—
		5p	1	1.5	Pseudopotential	—
		4d	2	1.5	Pseudopotential	—
		4d	2	2.5	Pseudopotential	—
48	Cd	5s	0	0.5	Pseudopotential	—
		5p	1	0.5	Pseudopotential	—
		5p	1	1.5	Pseudopotential	—
		4d	2	1.5	Pseudopotential	—
49	In	4d	2	2.5	Pseudopotential	—
		5s	0	0.5	Pseudopotential	—
		5p	1	0.5	Pseudopotential	—
		5p	1	1.5	Pseudopotential	—
50	Sn	4d	2	1.5	Pseudopotential	—
		4d	2	2.5	Pseudopotential	—
		5s	0	0.5	Pseudopotential	—
		5p	1	0.5	Pseudopotential	—
51	Sb	5p	1	1.5	Pseudopotential	—
		5p	1	0.5	Pseudopotential	—
		5s	0	0.5	Pseudopotential	—
52	Te	5p	1	0.5	Pseudopotential	—
		5p	1	1.5	Pseudopotential	—
53	I	5s	0	0.5	Pseudopotential	—
		5p	1	0.5	Pseudopotential	—
		5p	1	1.5	Pseudopotential	—
54	Xe	5s	0	0.5	Pseudopotential	—
		5p	1	0.5	Pseudopotential	—
		5p	1	1.5	Pseudopotential	—
		4d	2	1.5	Pseudopotential	—
55	Cs	4d	2	2.5	Pseudopotential	—
		5s	0	0.5	Pseudopotential	—
		6s	0	0.5	Pseudopotential	—
		5p	1	0.5	Pseudopotential	—
		5p	1	1.5	Pseudopotential	—
		5d	2	1.5	OpenMX Fitting	3.566
		5d	2	2.5	OpenMX Fitting	3.566
56	Ba	5d	2	2.5	OpenMX Fitting	3.039
		5d	2	1.5	OpenMX Fitting	3.039
		5p	1	0.5	Pseudopotential	—
		5p	1	1.5	Pseudopotential	—
		6s	0	0.5	Pseudopotential	—
		5s	0	0.5	Pseudopotential	—
		5p	1	0.5	Pseudopotential	—
72	Hf	5p	1	1.5	Pseudopotential	—
		5d	2	1.5	Pseudopotential	—
		5d	2	2.5	Pseudopotential	—
		6p	1	0.5	Orthogonalization	4.400
		6p	1	1.5	Orthogonalization	3.900
		5s	0	0.5	Pseudopotential	—
		6s	0	0.5	Pseudopotential	—
73	Ta	5p	1	0.5	Pseudopotential	—
		5p	1	1.5	Pseudopotential	—
		6p	1	1.5	Pseudopotential	—
		5d	2	1.5	Pseudopotential	—
		5d	2	2.5	Pseudopotential	—
		5s	0	0.5	Pseudopotential	—
		6s	0	0.5	Pseudopotential	—

Z	Element	Orbital l	j	Source	$\alpha(\text{bohr}^{-1})$
74	W	5s	0	0.5 Pseudopotential	—
		6s	0	0.5 Pseudopotential	—
		5p	1	0.5 Pseudopotential	—
		6p	1	0.5 Pseudopotential	—
		5p	1	1.5 Pseudopotential	—
		6p	1	1.5 Pseudopotential	—
		5d	2	1.5 Pseudopotential	—
		5d	2	2.5 Pseudopotential	—
75	Re	5s	0	0.5 Pseudopotential	—
		6s	0	0.5 Pseudopotential	—
		5p	1	0.5 Pseudopotential	—
		5p	1	1.5 Pseudopotential	—
		5d	2	1.5 Pseudopotential	—
		5d	2	2.5 Pseudopotential	—
		6p	1	0.5 Orthogonalization	4.900
		6p	1	1.5 Orthogonalization	4.500
76	Os	5s	0	0.5 Pseudopotential	—
		6s	0	0.5 Pseudopotential	—
		5p	1	0.5 Pseudopotential	—
		5p	1	1.5 Pseudopotential	—
		5d	2	1.5 Pseudopotential	—
		5d	2	2.5 Pseudopotential	—
		6p	1	0.5 Orthogonalization	5.100
		6p	1	1.5 Orthogonalization	4.600
77	Ir	6s	0	0.5 Pseudopotential	—
		6p	1	0.5 Pseudopotential	—
		6p	1	1.5 Pseudopotential	—
		5d	2	1.5 Pseudopotential	—
		5d	2	2.5 Pseudopotential	—
78	Pt	6s	0	0.5 Pseudopotential	—
		6p	1	0.5 Pseudopotential	—
		6p	1	1.5 Pseudopotential	—
		5d	2	1.5 Pseudopotential	—
		5d	2	2.5 Pseudopotential	—
79	Au	6s	0	0.5 Pseudopotential	—
		6p	1	0.5 Pseudopotential	—
		6p	1	1.5 Pseudopotential	—
		5d	2	1.5 Pseudopotential	—
		5d	2	2.5 Pseudopotential	—
80	Hg	6s	0	0.5 Pseudopotential	—
		6p	1	0.5 Pseudopotential	—
		6p	1	1.5 Pseudopotential	—
		5d	2	1.5 Pseudopotential	—
		5d	2	2.5 Pseudopotential	—
81	Tl	6s	0	0.5 Pseudopotential	—
		6p	1	0.5 Pseudopotential	—
		6p	1	1.5 Pseudopotential	—
		5d	2	1.5 Pseudopotential	—
		5d	2	2.5 Pseudopotential	—
82	Pb	6s	0	0.5 Pseudopotential	—
		6p	1	0.5 Pseudopotential	—
		6p	1	1.5 Pseudopotential	—
		5d	2	1.5 Pseudopotential	—
		5d	2	2.5 Pseudopotential	—
83	Bi	6s	0	0.5 Pseudopotential	—
		6p	1	0.5 Pseudopotential	—
		6p	1	1.5 Pseudopotential	—
		5d	2	1.5 Pseudopotential	—

Z	Element	Orbital l	j	Source	$\alpha(\text{bohr}^{-1})$
84	Po	6s	0	0.5 Pseudopotential	—
		6p	1	0.5 Pseudopotential	—
		6p	1	1.5 Pseudopotential	—
		5d	2	1.5 Pseudopotential	—
		5d	2	2.5 Pseudopotential	—
85	At	6s	0	0.5 Pseudopotential	—
		6p	1	0.5 Pseudopotential	—
		6p	1	1.5 Pseudopotential	—
		5d	2	1.5 Pseudopotential	—
86	Rn	5d	2	2.5 Pseudopotential	—
		6s	0	0.5 Pseudopotential	—
		6p	1	0.5 Pseudopotential	—
		6p	1	1.5 Pseudopotential	—
87	Fr	5d	2	1.5 Pseudopotential	—
		5d	2	2.5 Pseudopotential	—
		6s	0	0.5 Pseudopotential	—
		7s	0	0.5 Pseudopotential	—
		6p	1	0.5 Pseudopotential	—
88	Ra	6p	1	1.5 Pseudopotential	—
		5d	2	1.5 Pseudopotential	—
		5d	2	2.5 Pseudopotential	—
		6s	0	0.5 Pseudopotential	—
		7s	0	0.5 Pseudopotential	—

SUPPLEMENTARY TABLE VIII: Values of α and minimal set of orbitals for projectors from **OpenMX** fitting. We note that we only report values for those orbitals for which a value was fitted from OpenMX in this work (i.e., for orbitals that were not included in the PAOs for at least one pseudopotential family, and that did not have underlying orbitals with the same angular character, so that no orthogonality condition on the radial part could be enforced).

Z	Element	Filename	Orbital	l	$\alpha(\text{bohr}^{-1})$
1	H	H5.0.pao	1s	0	1.075
2	He	He10.0.pao	1s	0	1.529
3	Li	Li12.0.pao	2s	0	2.520
			2p	1	1.114
4	Be	Be8.0.pao	2s	0	0.649
			2p	1	1.834
5	B	B9.0.pao	2s	0	0.833
			2p	1	2.143
6	C	C6.0.pao	2s	0	1.000
			2p	1	2.684
7	N	N6.0p.pao	2s	0	1.227
			2p	1	3.228
8	O	O6.0.pao	2s	0	1.412
			2p	1	3.755
9	F	F7.0.pao	2s	0	1.608
			2p	1	4.230
10	Ne	Ne11.0.pao	2s	0	1.797
			2p	1	4.748
11	Na	Na11.0.pao	3s	0	2.072
			3p	1	5.830
12	Mg	Mg7.0.pao	3s	0	0.587
			3p	1	6.876
13	Al	Al7.0.pao	3s	0	0.682
			3p	1	1.768
14	Si	Si8.0.pao	3s	0	0.765
			3p	1	1.876
15	P	P8.0.pao	3s	0	0.886
			3p	1	2.191
16	S	S9.0.pao	3s	0	0.992
			3p	1	2.432
17	Cl	Cl7.0.pao	3s	0	1.096
			3p	1	2.733
18	Ar	Ar11.0.pao	3s	0	1.197
			3p	1	3.001
19	K	K12.0.pao	4s	0	1.336
			3d	2	2.727
20	Ca	Ca9.0.pao	4s	0	1.474
			3d	2	3.983
21	Sc	Sc11.0.pao	4s	0	1.589
			4p	1	4.353
			3d	2	5.200
22	Ti	Ti11.0.pao	4s	0	1.698
			4p	1	4.628
			3d	2	5.246
23	V	V8.0.pao	4s	0	1.796
			4p	1	4.925
			3d	2	5.774
24	Cr	Cr6.0.pao	4s	0	1.902
			4p	1	5.222
			3d	2	6.565
25	Mn	Mn8.0.pao	4s	0	1.999
			4p	1	5.603
			3d	2	8.113

Z	Element	Filename	Orbital	l	$\alpha(\text{bohr}^{-1})$
26	Fe	Fe6.0S.pao	4s	0	0.641
			4p	1	5.882
			3d	2	8.140
27	Co	Co8.0H.pao	4s	0	2.195
			4p	1	6.180
			3d	2	8.453
28	Ni	Ni10.0H.pao	4s	0	2.321
			4p	1	6.481
			3d	2	8.893
29	Cu	Cu8.0S.pao	4s	0	0.601
			4p	1	2.149
			3d	2	9.296
30	Zn	Zn10.0S.pao	4s	0	0.628
			4p	1	1.361
			3d	2	10.651
31	Ga	Ga7.0.pao	4s	0	0.729
			4p	1	1.781
32	Ge	Ge9.0.pao	4s	0	0.798
			4p	1	1.815
33	As	As9.0.pao	4s	0	0.875
			4p	1	2.035
34	Se	Se7.0.pao	4s	0	0.947
			4p	1	2.272
35	Br	Br7.0.pao	4s	0	1.018
			4p	1	2.447
36	Kr	Kr10.0.pao	4s	0	1.087
			4p	1	2.612
37	Rb	Rb13.0.pao	5s	0	1.182
			4d	2	2.197
38	Sr	Sr12.0.pao	5s	0	1.275
			4d	2	4.400
39	Y	Y10.0.pao	5s	0	1.348
			5p	1	3.560
			4d	2	3.758
40	Zr	Zr9.0.pao	5s	0	1.430
			5p	1	3.760
			4d	2	4.062
41	Nb	Nb9.0.pao	5s	0	1.505
			5p	1	3.981
			4d	2	4.590
42	Mo	Mo7.0.pao	5s	0	1.567
			5p	1	4.190
			4d	2	5.150
43	Tc	Tc11.0.pao	5s	0	1.641
			5p	1	4.411
			4d	2	5.645
44	Ru	Ru7.0.pao	5s	0	0.569
			5p	1	4.599
			4d	2	5.920
45	Rh	Rh9.0.pao	5s	0	0.534
			5p	1	4.800
			4d	2	6.305
46	Pd	Pd11.0.pao	5s	0	0.522
			5p	1	4.966
			4d	2	6.254
47	Ag	Ag9.0.pao	5s	0	0.547
			5p	1	5.191
			4d	2	7.107
48	Cd	Cd7.0.pao	5s	0	0.621
			5p	1	1.815
			4d	2	7.835

Z	Element	Filename	Orbital	l	$\alpha(\text{bohr}^{-1})$
49	In	In7.0.pao	5s	0	0.668
			5p	1	1.684
50	Sn	Sn9.0.pao	5s	0	0.713
			5p	1	1.652
51	Sb	Sb11.0.pao	5s	0	0.771
			5p	1	1.791
52	Te	Te9.0.pao	5s	0	0.825
			5p	1	1.946
53	I	I7.0.pao	5s	0	0.879
			5p	1	2.144
54	Xe	Xe13.0.pao	5s	0	0.930
			5p	1	2.230
55	Cs	Cs12.0.pao	6s	0	1.001
			5d	2	3.566
56	Ba	Ba10.0.pao	6s	0	1.069
			5d	2	3.039
			6s	0	1.544
72	Hf	Hf11.0.pao	6p	1	3.885
			5d	2	4.081
73	Ta	Ta11.0.pao	6s	0	1.593
			6p	1	4.070
			5d	2	4.551
74	W	W7.0.pao	6s	0	0.577
			6p	1	4.137
			5d	2	4.789
75	Re	Re7.0.pao	6s	0	1.698
			6p	1	4.338
			5d	2	5.392

Z	Element	Filename	Orbital	l	$\alpha(\text{bohr}^{-1})$
76	Os	Os7.0.pao	6s	0	0.600
			6p	1	4.490
77	Ir	Ir11.0.pao	5d	2	5.623
			6s	0	0.576
			6p	1	4.615
78	Pt	Pt9.0.pao	5d	2	5.716
			6s	0	0.590
			6p	1	4.758
79	Au	Au11.0.pao	5d	2	5.988
			6s	0	0.589
			6p	1	4.873
80	Hg	Hg8.0.pao	5d	2	6.301
			6s	0	0.638
			6p	1	5.073
81	Tl	Tl8.0.pao	5d	2	6.837
			6s	0	0.689
82	Pb	Pb8.0.pao	6p	1	5.245
			6s	0	0.742
83	Bi	Bi8.0.pao	6p	1	1.666
			6s	0	0.792
84	Po	Po10.0.pao	6p	1	1.786
			6s	0	0.839
86	Rn	Rn13.0.pao	6p	1	1.850
			6s	0	0.934
			6p	1	2.091

-
- [1] J. Qiao, G. Pizzi, and N. Marzari, Projectability disentanglement for accurate and automated electronic-structure Hamiltonians, *npj Computational Materials* **9**, 208 (2023).
 - [2] S. V. Gallego, J. M. Perez-Mato, L. Elcoro, E. S. Tasci, R. M. Hanson, K. Momma, M. I. Aroyo, and G. Madariaga, MAGNDATA : towards a database of magnetic structures. I. The commensurate case, *Journal of Applied Crystallography* **49**, 1750 (2016).
 - [3] T. Ozaki, Variationally optimized atomic orbitals for large-scale electronic structures, *Physical Review B* **67**, 155108 (2003).
 - [4] Suggested pseudopotentials, https://dalcorsio.github.io/pslibrary/PP_list.html, online; accessed 20 January 2025.

